JAMES | Journal of Advances in Modeling Earth Systems

RESEARCH ARTICLE
10.1029/2019MS001646

This article is a companion to Sein et al. (2015), https://doi.org/10.1002/2014MS000357.

Key Points:
- The regionally coupled model shows reduced oceanic biases in the North Atlantic and a better simulation of the atmospheric circulation
- The Arctic reaches a seasonally ice-free state by 2055 with the regionally coupled model under RCP8.5 scenario
- Changes in biogeochemistry are generally stronger and show enhanced details in the regionally coupled model

Correspondence to:
D. V. Sein,
dmitry.sein@awi.de

Citation:
Sein, D. V., Gröger, M., Cabos, W., Alvarez-Garcia, F. J., Hagemann, S., Pinto, J. G., et al. (2020). Regionally coupled atmosphere-ocean-marine biogeochemistry model ROM: 2. Studying the climate change signal in the North Atlantic and Europe. *Journal of Advances in Modeling Earth Systems*, *12*, e2019MS001646. https://doi.org/10.1029/2019MS001646

Received 20 MAR 2019
Accepted 23 JUN 2020
Accepted article online 29 JUN 2020

Regionally Coupled Atmosphere-Ocean-Marine Biogeochemistry Model ROM: 2. Studying the Climate Change Signal in the North Atlantic and Europe

Dmitry V. Sein[1,2], Matthias Gröger[3], William Cabos[4], Francisco J. Alvarez-Garcia[4], Stefan Hagemann[5], Joaquim G. Pinto[6], Alfredo Izquierdo[7], Alba de la Vara[8,9], Nikolay V. Koldunov[1,10], Anton Yu. Dvornikov[2], Natalia Limareva[11], Evgenia Alekseeva[2], Benjamin Martinez-Lopez[12], and Daniela Jacob[13]

[1]Alfred Wegener Institute for Polar and Marine Research, Bremerhaven, Germany, [2]P. P. Shirshov Institute of Oceanology RAS, Moscow, Russia, [3]Leibniz Institute for Baltic Sea Research Warnemünde, Rostock, Germany, [4]Department of Physics and Mathematics, University of Alcala, Alcala de Henares, Spain, [5]Institute of Coastal Research, Helmholtz-Zentrum Geesthacht, Geesthacht, Germany, [6]Institute of Meteorology and Climate Research, Karlsruhe Institute of Technology, Karlsruhe, Germany, [7]Instituto Universitario de Investigación Marina (INMAR), University of Cádiz, Puerto Real, Spain, [8]Environmental Sciences Institute, University of Castilla-La Mancha, Toledo, Spain, [9]Departamento de Matemática Aplicada a la Ingeniería Industrial, E.T.S.I. Industriales, Universidad Politécnica de Madrid, Madrid, Spain, [10]MARUM – Center for Marine Environmental Sciences, Bremen, Germany, [11]The Institute of Service, Tourism and Design. North Caucasus Federal University, Stavropol, Russia, [12]Centro de Ciencias de la Atmósfera, Universidad Nacional Autónoma de México, Mexico City, Mexico, [13]Climate Service Center Germany (GERICS), Hamburg, Germany

Abstract Climate simulations for the North Atlantic and Europe for recent and future conditions simulated with the regionally coupled ROM model are analyzed and compared to the results from the MPI-ESM. The ROM simulations also include a biogeochemistry and ocean tides. For recent climate conditions, ROM generally improves the simulations compared to the driving model MPI-ESM. Reduced oceanic biases in the Northern Atlantic are found, as well as a better simulation of the atmospheric circulation, notably storm tracks and blocking. Regarding future climate projections for the 21st century following the RCP 4.5 and 8.5 scenarios, MPI-ESM and ROM largely agree qualitatively on the climate change signal over Europe. However, many important differences are identified. For example, ROM shows an SST cooling in the Subpolar Gyre, which is not present in MPI-ESM. Under the RCP8.5 scenario, ROM Arctic sea ice cover is thinner and reaches the seasonally ice-free state by 2055, well before MPI-ESM. This shows the decisive importance of higher ocean resolution and regional coupling for determining the regional responses to global warming trends. Regarding biogeochemistry, both ROM and MPI-ESM simulate a widespread decline in winter nutrient concentration in the North Atlantic of up to ~35%. On the other hand, the phytoplankton spring bloom in the Arctic and in the North-Western Atlantic starts earlier, and the yearly primary production is enhanced in the Arctic in the late 21st century. These results clearly demonstrate the added value of ROM to determine more detailed and more reliable climate projections at the regional scale.

Plain Language Summary We downscale present climate and future climate change projections for the North Atlantic and Europe using a regionally coupled Earth System Model including atmosphere, ocean, river runoff, and ocean biogeochemistry components. This approach allows us to attain higher spatial resolution and to a more accurate representation of key physical processes, yielding a better simulation of present climate at regional and local scales when compared to the driving global climate model. Future climate change projections show more detail at regional and local scale, mostly related to the improvement in the representation of orography and bathymetry. These improvements along with a better representation of the interactive ocean-atmosphere coupling lead to other remarkable differences with the driving global climate model: (1) colder Sea Surface Temperature in the Subpolar Gyre region, indicating a local convection collapse and a Atlantic Meridional Overturning Circulation slowdown; (2) a seasonal free-ice Arctic is reached by 2055 under RCP8.5 scenario, well before projected by the driving global climate model; and (3) stronger reduction in nutrients in the North Atlantic by the end of the 21st century. These results clearly

demonstrate the added value of the regionally coupled model system to determine more reliable climate projections at the regional scale.

1. Introduction

The North Atlantic (NA) atmosphere-ocean system plays a key role in global climate change and variability (Collins et al., 2018; Jackson et al., 2015; Monerie et al., 2019; Ting et al., 2011; R. Zhang et al., 2019). In the atmosphere, the NA features a quasi-stationary jet stream blowing from North America to the European continent, and the so-called "storm track," a zonally oriented region defined by the frequent eastbound passage of synoptic-scale disturbances (e.g., Shaw et al., 2016). Changes in these elements are modulated by the NA Oscillation, the most prominent mode of variability in the region (see Hurrell et al., 2003). This and other relevant circulation patterns, such as the East Atlantic pattern (Moore & Renfrew, 2012), together with the air-sea interaction over the region, strongly influence the European climate. Surface temperature anomalies over the continent originate from fluctuations in the intensity and position of the prevalent westerly winds, and variations in the storm track exert a pronounced impact on the precipitation pattern over Europe. As to the ocean, the NA constitutes a fundamental branch of the deep water circulation, as it comprises the source area of NA Deep Water, with main deep water convection sites in the Labrador Sea and the Norwegian-Greenland Sea. The Atlantic Meridional Overturning circulation (AMOC) imposes not only a strong imprint on the global deep water ventilation but likewise influences global climate change through a number of processes. It plays an essential role in the meridional transport of heat and heat uptake of the ocean. It further modulates the decadal climate variability of the Gulf Stream-Subpolar Gyre (SPG) system, which is important for the climate of Northern Europe. In turn, the NA overturning is also known to be very sensitive against freshwater fluxes and air temperature anomalies (e.g., Swingedouw et al., 2009; Zhang, 2017). Such sensitivity makes this region vulnerable to climate change, thus increasing its potential to feed back to global climate (Rahmstorf et al., 2015). Therefore, a correct representation of the AMOC is crucial for the simulated climate in the NA and for climate variability over different parts of the world. Additionally, the NA and the NW European shelf have an important role in the marine carbon cycle, the NA being a major sink for atmospheric carbon. A large part of carbon uptake in the NA occurs regularly during the pronounced phytoplankton bloom in spring, which fixes carbon into organic soft tissue due to photosynthesis. This lowers the partial pressure of carbon dioxide (pCO2) of the surface water, which facilitates the air-to-sea carbon flux. The following export of dead phytoplankton (detritus) to the deep ocean effectively removes carbon from the atmosphere (carbon pump). The timing of the spring bloom in the NA is strongly related to the atmospheric and oceanic physical conditions, in particular to stratification (Sverdrup, 1953) and vertical mixing (Behrenfeld, 2010). Northward heat transport by oceanic eddies in the NA significantly acts upon these factors, modifying the seasonal stratification 20 to 30 days in advance than would be expected from surface warming alone (Mahadevan et al., 2012).

The role of shelf regions in the global carbon cycle is presently a matter of debate. While it was postulated that shelves could account for 20% to 50% of the total oceanic uptake (Thomas et al., 2004; Tsunogai et al., 1999), recent studies suggest they could have acted as a source and only shortly ago turned into a sink (e.g., Laruelle et al., 2018). Further evidence exists that especially middle- to high-latitude shelves may serve as a net sink for carbon dioxide while low-latitude regions may serve rather as a source (Cai, 2011). The NW European shelf, in particular, has been shown to be a large sink for atmospheric carbon (Bozec et al., 2005; Gröger et al., 2013; Holt et al., 2009; Thomas et al., 2004, 2005), but there is a large uncertainty as to its response to global warming in the next decades, mostly associated with the impact of possible changes in primary production.

Currently, most climate change information for the NA region and its feedback to global climate change relies on the global climate models (GCMs). Those models have relatively low horizontal resolutions and are not able to capture some key physical phenomena, thus hampering the accuracy of climate projections on regional and local scales (Marotzke et al., 2016; Xie et al., 2015), especially in the NA, where high resolution is necessary for both the oceanic and atmospheric components. High atmospheric resolution is needed to improve the representation of the jet stream and blocking weather situations (Jung et al., 2012) in the NA. A higher resolution also amplifies the storm-track response to global warming and leads to enhanced

extratropical cyclone activity that is most evident in the northeast NA. In the ocean, a realistic simulation of key components of the AMOC, as the SPG, the position of the NA Current and the Gulf Stream separation (e.g., Sein et al., 2018) also demands high resolution (e.g., Buckley & Marshall, 2016; Hirschi et al., 2020). The processes shaping the role of the NA and the NW European shelf in the global carbon cycle also require sufficient spatial detail. It has recently been shown (Gröger et al., 2015, 2019) that interactive coupling can have a large impact on local oceanographic parameters such as the Mixed Layer Depth (MLD). This would likewise influence the biogeochemical cycle.

In this work we explore the impact of the use of a regional coupled framework with a resolution higher than state-of-the-art global coupled models on the climate change signal in the NA. To this end, we use the high-resolution, regionally coupled model ROM (Sein et al., 2015). Previous studies (Cabos et al., 2019, 2020; Paxian et al., 2016; Sein et al., 2014) showed that ROM can improve the representation of key climate variables derived from the global forcing model in simulations of the present climate. Regarding climate change studies, ROM can simulate a climate change signal that is nontrivially different from the one simulated by the driving model (Bülow et al., 2014; Limareva et al., 2017). For instance, Limareva et al. (2017) found that the ROM climate change signal can be quite different from that simulated by the driving MPI-ESM model: A better resolved Great Caucasus mountain range leads to different temperature and precipitation responses in the South and North Caucasus, with stronger warming and drying in the former, in contrast to a homogenous climate change signal for both regions in MPI-ESM. Moreover, a biogeochemistry model is coupled to ROM, in a configuration that has not been applied before to the study of the NW shelf. Compared to other works on the NW shelf biogeochemistry, our setup combines a high spatial resolution, inclusion of the NA, and explicit consideration of interactive air-sea coupling of heat and momentum fluxes, whose effects on the biogeochemistry of the region have not yet been investigated, to our knowledge. Here we use the same configuration of the coupled system used in Sein et al. (2015) in order to provide further evidence that the adequate use of the advantages of higher resolution in regional coupling leads to additional, physically meaningful information in the simulated climate compared to the driving GCMs in climate change projections for Europe and the NA. From the four representative concentration pathways (RCPs; Van Vuuren et al., 2011) that were used for climate modeling and research for the IPCC fifth Assessment Report, we use RCP4.5 and RCP8.5. Thus, we consider one medium stabilization scenario and the high emission scenario. The key scientific questions are as follows:

1. Does ROM provide a clear added value compared to the global MPI-ESM model in terms of the representation of the atmospheric and oceanic circulations, thus reducing the biases compared to the Reanalysis?
2. Does ROM provide a different climate change signal at the regional scale compared to the global model, and if so, what are the key processes?
3. How do the physical changes in ROM influence the open ocean-shelf nutrient exchange, impact on the biogeochemistry on the NW European shelf, and mediate the response to climate change?

The study is organized as follows: After briefly introducing the ROM configuration used for the experiments presented here in section 2, section 3 reports the evaluation of the simulation of the present-time climate by ROM, highlighting both the model capabilities and remaining deficiencies in the simulation of the NA/European climate. The climate change signal for the 21st century is presented and discussed in section 4 based on projections following the RCP4.5 and RCP8.5 scenarios. Section 5 provides a summary and an outlook on future activities related to regional climate change studies with ROM.

2. Model Setup

In the configuration of ROM used in this work, the REgional atmosphere MOdel REMO (Jacob, 2001) with 37 km resolution and 27 hybrid vertical levels is coupled to the global ocean-sea ice-marine biogeochemistry model MPIOM/HAMOCC (Marsland et al., 2002) with increased resolution on the North-West European Shelf (up to 4 km in the German Bight). In addition, the ocean model was run with ocean tides. The coupled domain includes Europe, the North-East Atlantic, and part of the Arctic Ocean (Figure 1). The models are coupled via the OASIS coupler (Valke, 2006) with a good representation of the diurnal cycle (3 hr coupled time step). The 3 hr coupled frequency and the ocean tides make one of the major differences from the MPI-ESM CMIP5 simulations, where the diurnal cycle and tidal dynamics were neglected. Also, although ROM and MPI-ESM share the same oceanic component, their MPIOM setups are quite different. In MPI-

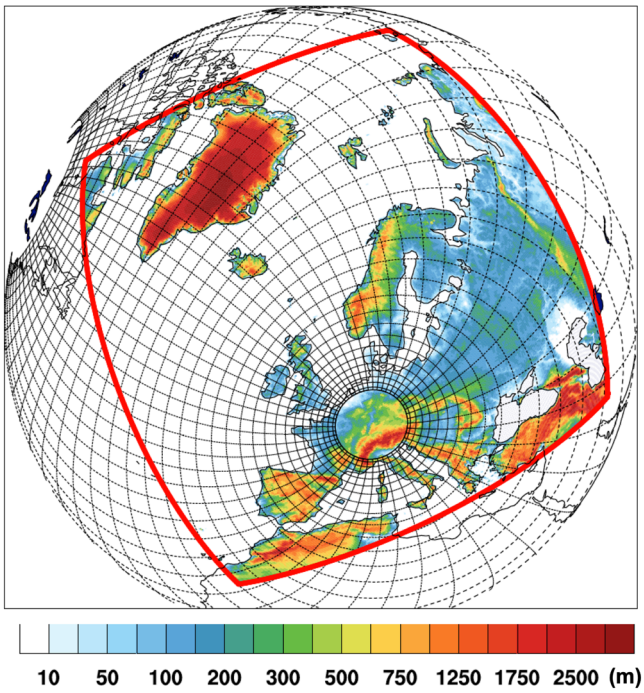

Figure 1. Grid configuration: The red rectangle contains the atmospheric domain (REMO model), where the atmosphere and the ocean are coupled. The black lines indicate the grid of the MPIOM ocean/sea ice and the HAMOCC biogeochemical models (only every 12th line is shown). Color scale represents orography (m) in the coupled area.

ESM, the poles of the orthogonal curvilinear coordinates are located over Greenland and inland of the Weddell Sea, with a minimum grid spacing of about 15 km around Greenland (Jungclaus et al., 2006). In ROM, the poles are placed over North America and Central Europe (see Figure 1), producing the higher resolution in the NA.

The ocean tidal forcing was derived from the full ephemeridic lunisolar tidal potential. The global Hydrological Discharge model HD, which calculates river runoff (0.5° horizontal grid resolution), is coupled to both the atmosphere and ocean components. Lateral atmospheric and upper oceanic boundary conditions outside the coupled domain were prescribed using MPI-ESM 20th century CMIP5 simulations, RCP4.5 and RCP8.5 scenarios data (the total simulation period was 1920–2005 + 2 × 2006–2100) for corresponding scenarios downscaling. The model spin-up covered the period 1920–2000. Then, the scenario runs (21st century) and, in parallel, a control run (20th century forcing) were carried out.

The use of a global ocean model allows us to avoid the complications related to the prescription of lateral boundary conditions. First, there are no inconsistencies between the regional model solution and the external data due to differences in resolution and physics and to the time interpolation. Second, the use of a global ocean model also allows trapped coastal waves (originating from outside the coupled domain) to influence the barotropic sea level variability and the bottom pressure in the coupled domain (Sein et al., 2015). In the atmospheric component, which is regional, the use of specific lateral boundary conditions may impact the simulated fields (see, e.g., Cabos et al., 2020).

The global oceanic component brings important advantages for climate change scenario simulations. For instance, it allows for the investigation of possible long-term changes in some oceanic extreme events (e.g., storm surges or floods in the North Sea). The common use of monthly mean data as a lateral boundary condition in regional ocean models makes this kind of study almost impossible.

With respect to the ocean carbon cycle, it is essential to spin up the model from an undisturbed preindustrial condition. This requires a preindustrial simulation in the order of several thousand years, which is impossible to do with the high-resolution coupled model used in this study. Thus, the spin-up was done using a cheaper model version where the ocean was forced with the corresponding pi-control run of the global MPI-ESM and in a coarser ocean resolution than used here. After ~4,000 years, ocean-atmosphere carbon fluxes varied around zero and were drift free. This run was then further prolonged for the whole historical period and several scenarios (Gröger et al., 2013). For the present study, initial ocean fields from 01.01.1920 were taken from the above-mentioned uncoupled coarse run to start the historical run and the following scenarios described in this study with the higher-resolution and interactively regionally coupled atmosphere model. The diagnosed ocean-atmosphere carbon fluxes have been compared in the first part of this study (Sein et al., 2015, Figure 3 therein). After a short expected spin-up period of a few decades, both model solutions are (after around 1970) indistinguishable from each other and show an oceanic carbon uptake of 1.6 Gt per year during the 1990s, which lies in the lower range of published values (Orr et al., 2005). Thus, the carbon cycle in this model can be considered quasi drift free (Sein et al., 2015). The same conclusion can be drawn with respect to other biogeochemical variables such as nutrients (see Sein et al., 2015, for more details).

3. Simulation of the Present-Time Climate

A detailed analysis of the ability of ROM to simulate the present-time (1980–1999 period) atmospheric, oceanic, and biogeochemical fields can be found in Sein et al. (2015). Given that here we study the climate change signal using a different global forcing (MPI-ESM instead of MPIOM/ECHAM5), we present a brief

evaluation of the most important features of atmospheric and oceanic fields for the 1976–2005 period below, which is considered as representative of the present-time climate in the CMIP5 simulations. In general, the biases for MPI-ESM and ROM are very similar to those found for ECHAM5/MPIOM and ROM, and thus, we only highlight the most relevant features of the validation. A detailed validation of the atmospheric, oceanic, and some biogeochemical fields not studied in Sein et al. (2015) can be found in the appendix.

3.1. The Atmosphere

ROM modifies the large-scale circulation biases in MPI-ESM, particularly for the summer. For example, ROM partially counterbalances the deficit in blocking frequency over the European continent and enhances cyclone activity over the eastern part of the continent. As a result, ROM is generally closer to observations (here ERA-Interim). Differences in atmospheric circulation also have an impact on the near-surface temperatures: ROM corrects the winter warm bias in MPI-ESM across much of Southern Europe (−0.5 and 1.6 K of mean bias, respectively) but enhances the cold bias over Scandinavia and Northern Russia (−2.8 and −0.6 K of mean bias, respectively). In summer, ROM reduces cold biases over Greenland (−0.03 vs. −3.2 K of mean bias) and emphasizes them over Scandinavia and Eastern Europe (−1.9 and −1.0 K of mean bias, respectively). Precipitation is also changed by the coupled dynamical downscaling: ROM reduces the MPI-ESM biases over most of the European continent but does not display a similar improvement over oceanic areas. The identified biases are broadly similar to the biases that are found when ROM is forced by MPIOM/ECHAM5 (Sein et al., 2015) but are in general weaker (cf. Appendix).

3.2. The Ocean and the Sea Ice

The higher MPIOM resolution in ROM contributes to provide a better representation of sea surface temperature (SST) and sea surface salinity (SSS) fields than in MPI-ESM. ROM corrects the reduced MPI-ESM meridional SST gradient in the northern NA. A more realistic NA current changes the strong warm bias in the Greenland-Iceland-Norwegian (GIN) seas present in MPI-ESM by a moderate cold bias and alleviates the strong cold bias in the NA (for instance, ROM has a −2.0 K bias in the region of the North Western corner, while the MPIESM bias is −3.9 K). The better reproduction of SST over the NA could explain the differences in large-scale atmospheric circulation, as the storm track location tends to be collocated with the areas of stronger meridional SST gradients. The different blocking frequencies could also be partially associated with these differences. Regarding the sea ice thickness (SIT), both MPI-ESM and ROM have, on average, thinner ice compared to PIOMAS reanalysis. However, in September ROM produces thicker ice in the Eurasian Basin of the Arctic Ocean, while in the spatial distribution of March SIT, ROM also has notably more sea ice along the Greenland shore and in the Barents Sea and is closer to PIOMAS over the central Arctic.

4. Future Climate Change (RCP4.5 and RCP8.5 Scenarios)

4.1. The Atmosphere

Figure 2 depicts mean sea level pressure (MSLP) changes between the period 2070–2099 and 1976–2005 in MPI-ESM and ROM according to the RCP4.5 and RCP8.5 scenarios. The spatial pattern over the Euro-Atlantic sector in all cases broadly agrees with those in the CMIP5 multimodel ensemble mean (Collins et al., 2013). Still, some features diverge: In the RCP8.5 experiments, the decrease over Scandinavia and eastern Europe extends westward into the subpolar NA, contrasting the enhancement displayed in that area by the CMIP5 ensemble mean (cf. Collins et al., 2013). In the summertime, the horseshoe-shaped region of increased MSLP that extends from Greenland to the Mediterranean Sea is shifted eastward compared to the CMIP5 ensemble mean, where it appears east of the British Isles.

ROM and MPI-ESM show a similar signal for the winds along the southern branch of the Icelandic Low, with substantial differences between both scenarios. For RCP4.5, the westerlies over the area are weakened, in connection with the extension of stronger MSLP from Greenland southward into the NA. On the other hand, the westerlies over this part of the NA are reinforced in RCP8.5, given the lower MSLP values in the region.

We can also identify differences in the climate change signal between both models. In ROM the amplitude and extension of the changes are generally weaker for both seasons. This leads to substantial differences in the modification of the surface winds over the domain (not shown), particularly in wintertime. These

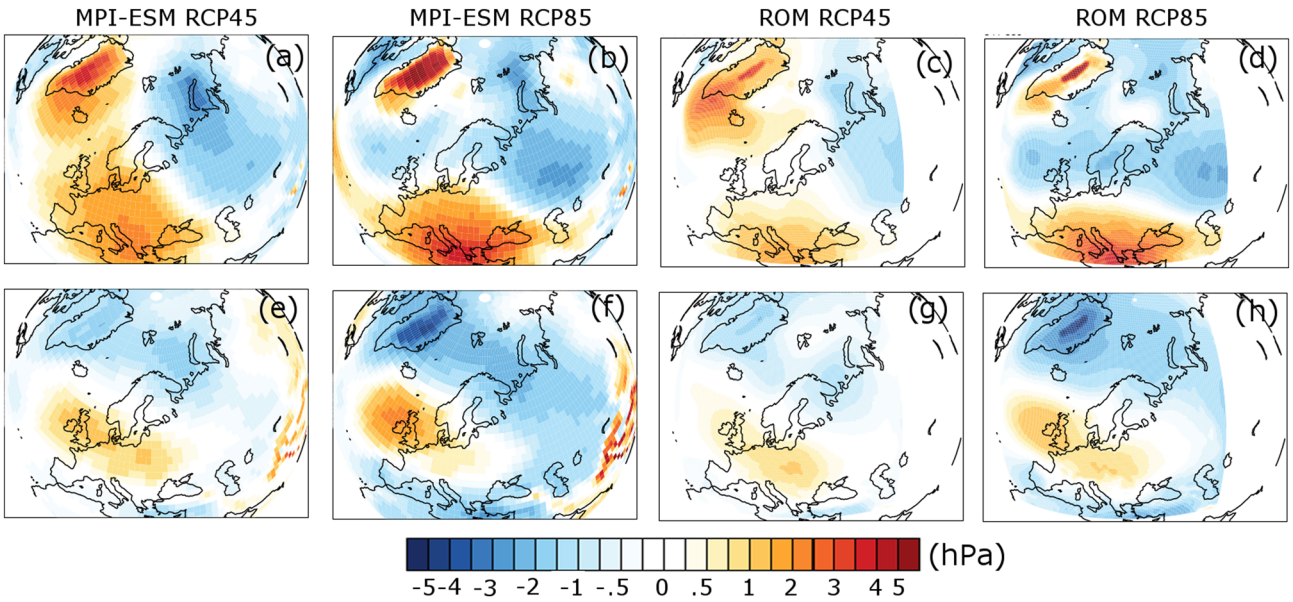

Figure 2. In the upper row, we show the differences in mean sea level pressure between the 2070–2099 and 1976–2005 periods in the DJF season for MPI-ESM under the (a) RCP4.5 and (b) RCP8.5 scenarios, and for ROM under the (c) RCP4.5 and (d) RCP8.5 scenarios. The lower row shows these differences for the JJA season for MPI-ESM under the (e) RCP4.5 and (f) RCP8.5 scenarios, and for ROM under the (g) RCP4.5 and (h) RCP8.5 scenarios.

differences are present in both RCPs, leading to a more moderate weakening of the westerlies over the western Mediterranean in ROM than MPI-ESM, and to stronger westerlies over much of the European continent.

Changes in 2-m temperature (T2M) between the 2070–2099 and 1976–2005 periods are displayed in Figure 3. The Arctic amplification can be identified in both scenarios and is similar for both models. However, the magnitude of the warming signal differs, in particular for Europe: The DJF warming under RCP4.5 (Figures 3a and 3c) is reduced by the downscaling, with about 1–2°C difference in Greenland, Scandinavia, Eastern Europe, and northern Russia. An exception is found off the eastern coast of Greenland, where ROM displays a remarkable warming, which is stronger than in MPI-ESM. The differences are less noticeable for RCP8.5 (Figures 3b and 3d). ROM is still warmer off East Greenland and shows slightly enhanced increases in temperature over some locations in central Europe and the Balkan Peninsula. In JJA the temperature changes in both models and scenarios (Figures 3e–3h) share the same pattern of stronger warming in southern Europe and in the northern band from Greenland to the Kara Sea, with a smaller, eastward growing warming in the intermediate latitude band. The pattern gains amplitude in the RCP8.5 pathway, particularly in MPI-ESM. Generally, the JJA warming is lower by about 1°C in ROM than in MPI-ESM. The stronger warming in RCP8.5 enhances the hydrological cycle in Eastern Europe up to 20–50%. These results show that the use of the regional configuration can lead to substantial modifications of the projected warming in regional terms. We speculate that the weaker warming in ROM is related to the impact on the atmospheric circulation of differences in the projected NA SST. The latter can be caused by better representation of mesoscale air-sea interaction (see, e.g., Hewitt et al., 2017). Differences arise mainly due to the ROM's higher resolution of both the atmosphere and the ocean in the region, which is already reflected in the present-time simulation. This issue deserves a more in-depth discussion, which will be presented in a forthcoming paper.

Changes in precipitation are shown in Figure 4. Under RCP4.5, only slight modifications are seen in DJF over most continental areas in both models (Figures 4a and 4c). Over the ocean the signal is stronger, with a rainfall increase over the Norwegian sea in MPI-ESM and a reduction in the northwestern NA in ROM. Changes over land areas are more noticeable and structured in JJA (Figures 4b and 4d), with drier conditions across Europe south of 55°N in both models. These changes are stronger in MPI-ESM, particularly over northern Russia. The RCP8.5 scenario features stronger changes in precipitation. DJF rainfall (Figures 4e–4h) increases in MPI-ESM and ROM throughout Northern Europe and diminishes in the

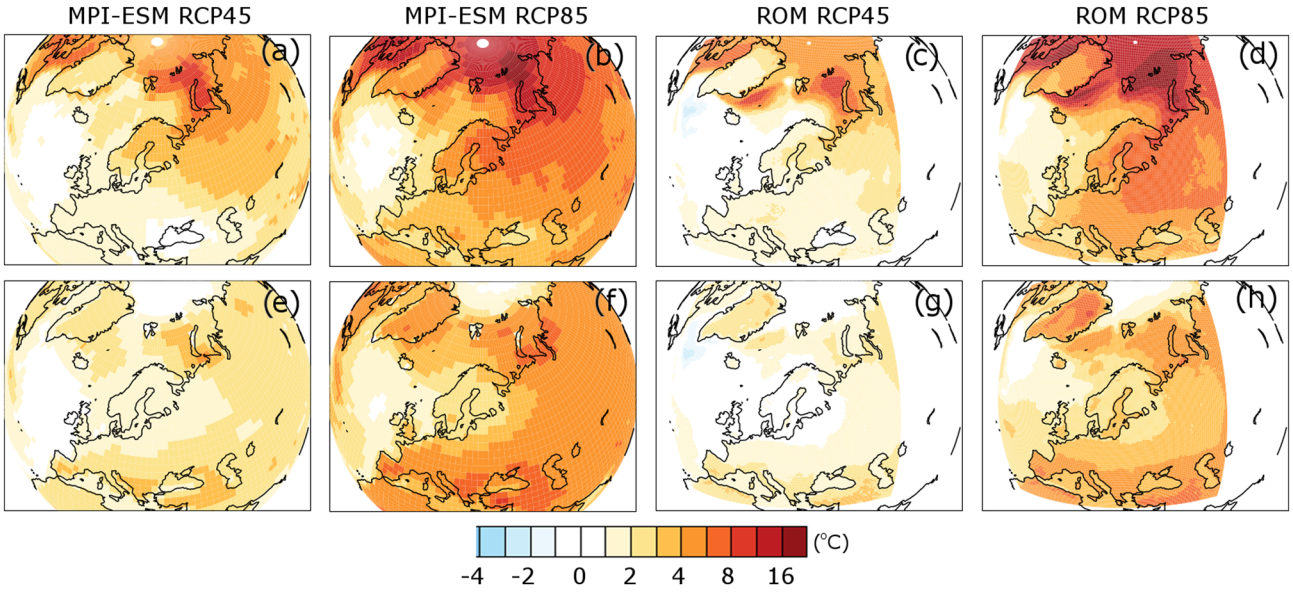

Figure 3. In the upper row, we represent the differences in 2-m temperature between the 2070–2099 and 1976–2005 periods in the DJF season for MPI-ESM under the (a) RCP4.5 and (b) RCP8.5 scenarios, and for ROM under the (c) RCP4.5 and (d) RCP8.5 scenarios. The lower row shows these differences for the JJA season for MPI-ESM under the (e) RCP4.5 and (f) RCP8.5 scenarios, and for ROM under the (g) RCP4.5 and (h) RCP8.5 scenarios.

Eastern Mediterranean. These changes are consistent with a shift of the storm tracks (Figures 5a–5h), identified in CMIP models as well (e.g., Ulbrich et al., 2008; Zappa, Shaffrey, Hodges, Sansom, et al., 2013), and with the reduced blocking frequency (Figure 5i and 5j) both in ROM and MPI ESM, again in agreement with other coupled models (Masato et al., 2013), also in terms of the maintenance of blocking occurrence in Eastern Europe (cf. Figure 5i). We observe a substantial reduction during summer in Southern Europe that already today experiences dry conditions like, for example, Spain. ROM shows here more spatial contours. This is extremely important for calculating water budgets along watersheds and to assess potential effects

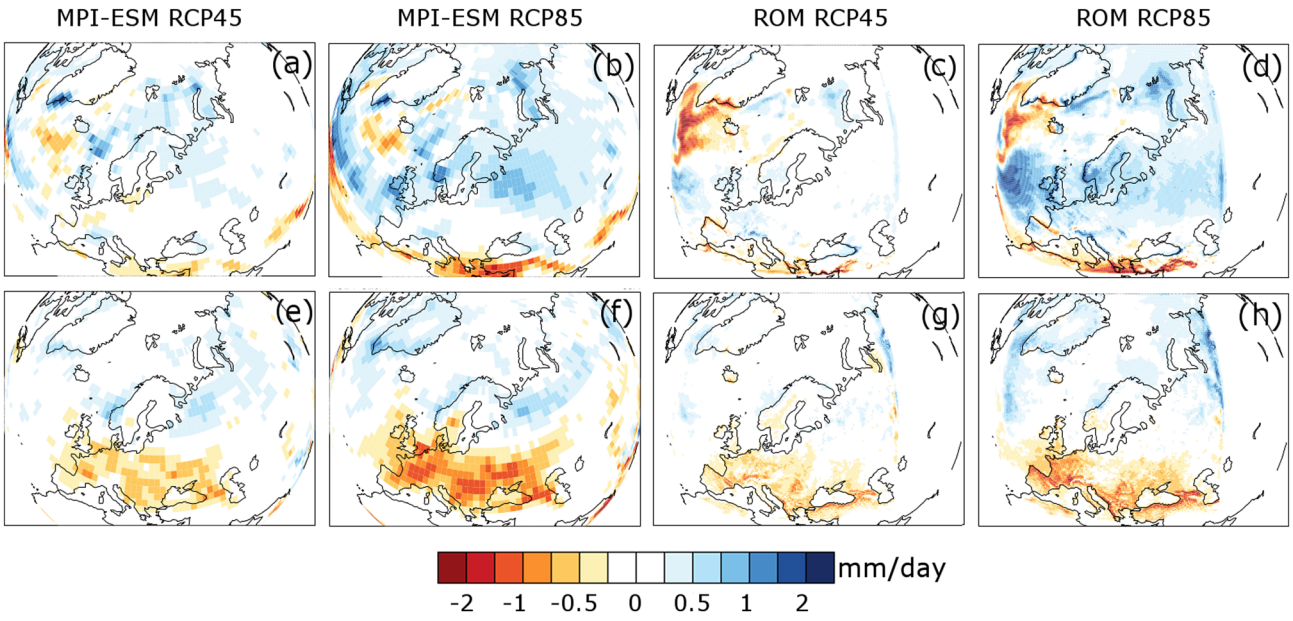

Figure 4. Changes in precipitation between the 2070–2099 and 1976–2005 periods in DJF (upper row) and JJA (lower row) for MPI-ESM under the (a and e) RCP4.5 and (b and f) RCP8.5 scenarios, and for ROM under the (c and g) RCP4.5 and (d and h) RCP8.5 scenarios.

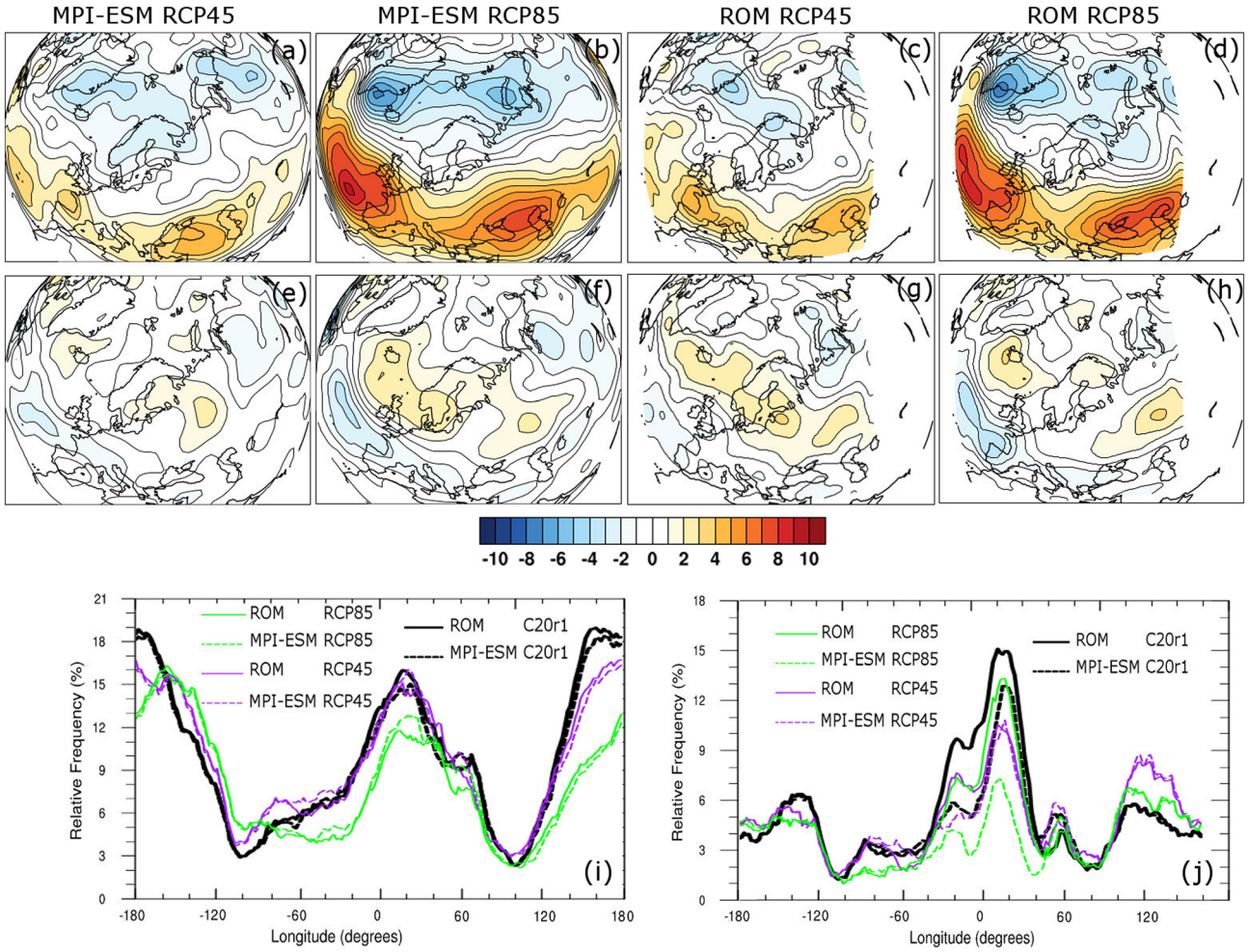

Figure 5. In the upper row we represent the differences in standard deviation of band-pass filtered (2.5–7 days) 500 hPa geopotential between the 2070–2099 and 1976–2005 periods in the DJF season for MPI-ESM under the (a) RCP4.5 and (b) RCP8.5 scenarios, and for ROM under the (c) RCP4.5 and (d) RCP8.5 scenarios. Middle row: same as upper row but for JJA. In this study, we use the same configuration of the coupled system in order to provide further evidence that the adequate use of the advantages of regional coupling and higher resolution leads to additional, physically meaningful information in the simulated climate compared to both GCMs and stand-alone atmospheric RCMs regarding climate change projections for Europe. Last row (i and j) shows the relative daily blocking frequency (after Tibaldi & Molteni, 1990) calculated on a daily basis. Panel (i) for winter (DJF) and (j) for summer (JJA).

for water-demanding industry and agriculture or to assess the effects on brackish ecosystems that are vulnerable to changes in water salinity like, for example, the Baltic Sea.

4.2. The Ocean and Arctic Sea Ice

SST changes between the period 2070–2099 and 1976–2005 in MPI-ESM and ROM according to the RCP4.5 and RCP8.5 scenarios are depicted in Figure 6. Both models show a general warming, which is stronger in RCP8.5, with increases of as much as 4 K. The cooling near Greenland clearly reflects the fingerprint of a weakening meridional overturning circulation in the Atlantic and has been used to estimate a three +/−1 Sv AMOC weakening or the most recent period (Caesar et al., 2018). The estimated SST trend for the associated dipole pattern was around 1.5 K per century, which is comparable to the SST climate change signal found in ROM (Figure 6), while the signal is smaller in MPI-ESM. In the following text, we further analyze the SST pattern in the NA to identify relevant processes.

In the RCP4.5 pathway, MPI-ESM presents the largest SST warming east of the Great Banks (between 35° and 45°N) and in the Greenland and Norwegian seas, while in the Eastern NA to the north of the SPG, changes in SST are negligible (a small SST decrease can be observed in some locations). In ROM, the warming patch of the Great Banks extends less to east and more to the south along the North America shelf break.

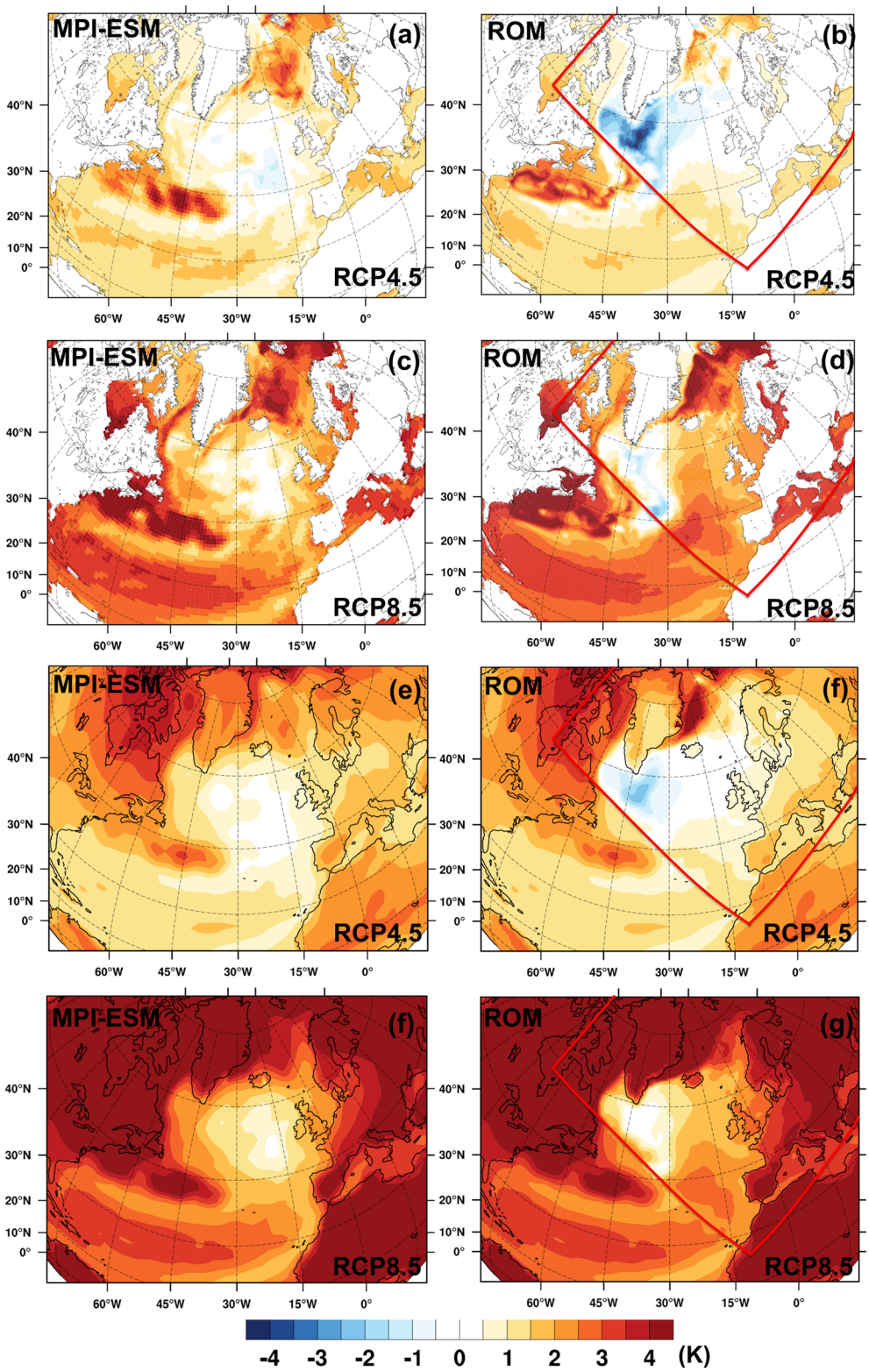

Figure 6. Mean SST change (a–d) and mean 2-m temperature change (e–f): (2070–2099) minus (1976–2005). In (f) and (g) ROM results are merged into MPI-ESM. The red line in panels (b), (d), (f), and (g) shows the coupled area.

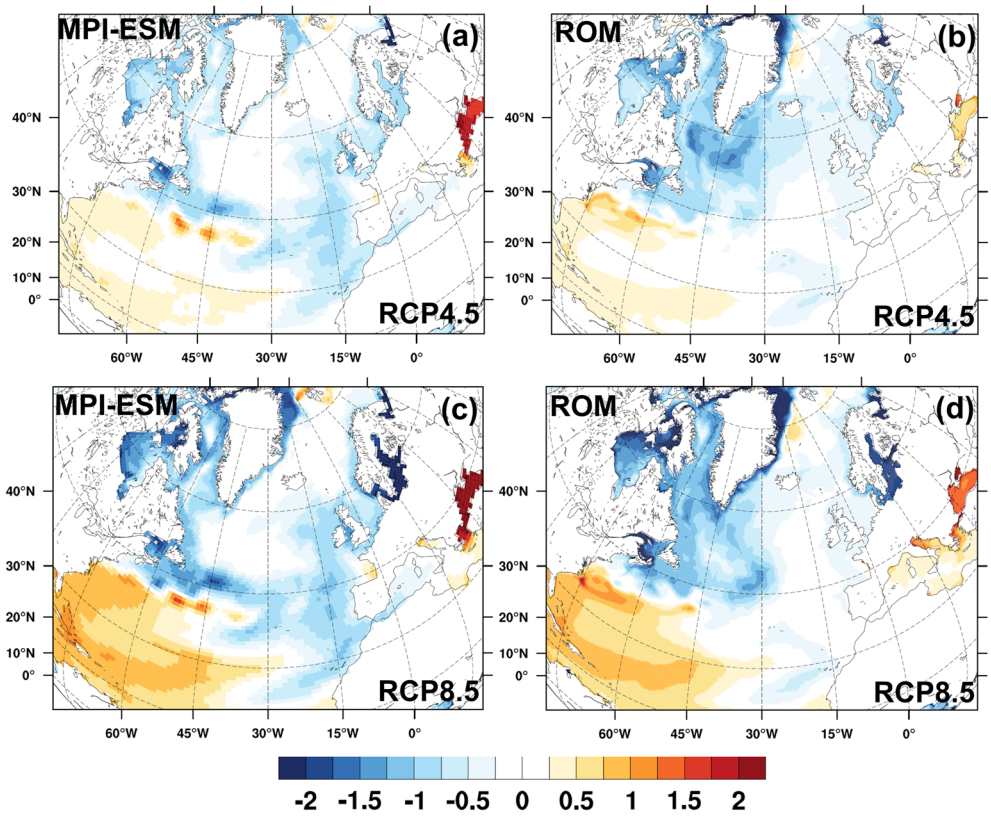

Figure 7. Mean SSS change (2070–2099) minus (1976–2005).

This is related to a further southward extension of the Labrador Current waters in ROM as compared to MPI-ESM (Sein et al., 2015). The maximum warming in the Norwegian Sea disappears, remaining only a subtle SST warming along NE Greenland coast. The most remarkable difference takes place within the SPG, where a cooling down to 3 K can be observed (Figure 6c). The MPI-ESM and ROM RCP8.5 runs depict the same spatial pattern in SST changes as their corresponding RCP4.5 runs, but with a greater general warming. As a result, the surface cooling simulated by ROM in the SPG almost vanishes and is replaced by a meridionally stretched area of nearly unchanged SST. This well-pronounced SST change pattern shown by ROM with cooling at the SPG and warming at the Gulf Stream region (more evident for RCP4.5) has been recently identified as a fingerprint of an AMOC slowdown on the basis of high-resolution model simulations by Caesar et al. (2018), as pointed out above.

The simulated SSS changes for RCP4.5 and RCP8.5 are shown in Figure 7. MPI-ESM simulates for RCP4.5 a very light (0.5–0.9) SSS increase to the SW of the NA and a freshening along the coasts from the Gulf of Maine to the north and throughout the Eastern NA, also more evident on the shelves. In turn, ROM shows almost no SSS changes in the Eastern NA, while it presents a clear freshening in the Western NA north of 45°N and with minimum values (−1.5) coincident with the areas of more pronounced SST cooling within the SPG shown in Figure 6b.

The strong SSS change signal into the Baltic Sea has the following explanation. For both scenarios, a substantial increase of river runoff into the Baltic Sea is projected (see Figure 15a) that is caused by an increase of precipitation over the Baltic Sea catchment. For RCP8.5, this increase is up to 30% during fall and winter compared to the end of the 20th century. The salinity in Baltic Sea was mainly balanced by the water exchange with the North Sea and river runoff from the Baltic Sea catchment. The first source (water exchange) has not been changed significantly because of its limitation by the Danish Straits topography. The second (river runoff) increases substantially, leading to the freshening of the basin as well as stronger sea level rise (Figure 11). Mean salinity there decreases by up to 4 psu in case of RCP8.5 scenario.

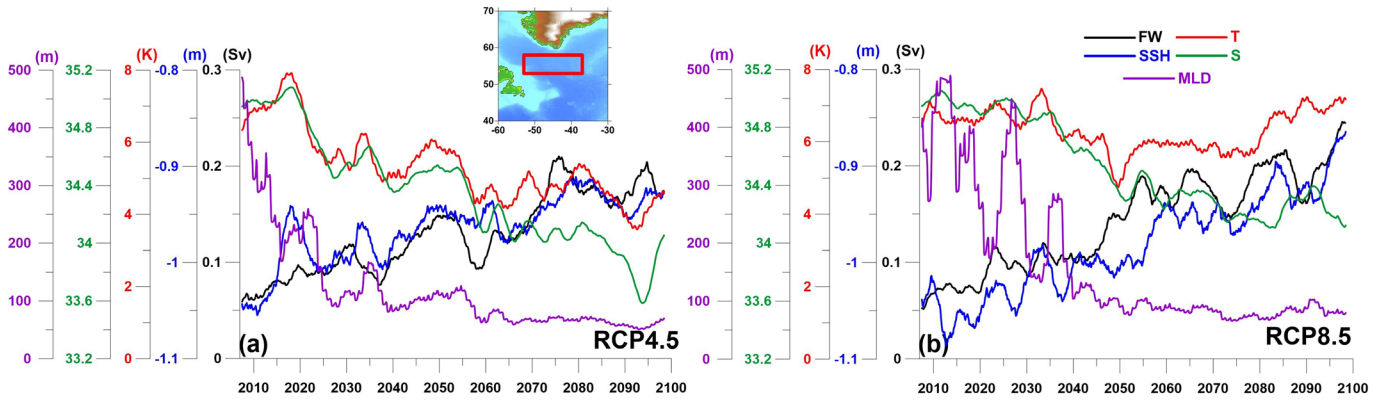

Figure 8. ROM freshwater flux through the Denmark Strait (FW), averaged over 37–53°W, 53–58°N (marked as a red box on the figure at the top) sea surface height (SSH), mixed layer depth (MLD), mean 0–80 m temperature (T), and salinity (S). All quantities are 3 year running mean.

However, due to the reduced exchange with the adjacent North Sea, any uncertainty in simulated runoff can have large effect on the mean salinity in this area. The processes described above cause stronger Baltic Sea level rise. It reaches up to 40 cm by the end of the 21st century (see Figures 11c and 11d), which is much larger compared to the North Sea (~25 cm).

The SSS changes for both MPI-ESM and ROM present the same spatial patterns under both pathways, but with larger increases/decreases under RCP8.5 (Figure 7). This fact can be related to the stronger radiative forcing, which induces two competing processes: an increase of evaporation (which may cause an SSS rise) and ice melting at high, northern latitudes (which may lower SSS). The balance between evaporation and ice melting, together with oceanic circulation, may cause the observed SSS pattern. As for SST changes, the most noticeable differences between MPI-ESM and ROM are mostly located in the SPG and in the Eastern NA.

Recently, Sgubin et al. (2017) assessed the performance of 40 climate models from CMIP5 under different emission scenarios and found different SST responses in the SPG. In the ensemble mean, the SPG appears

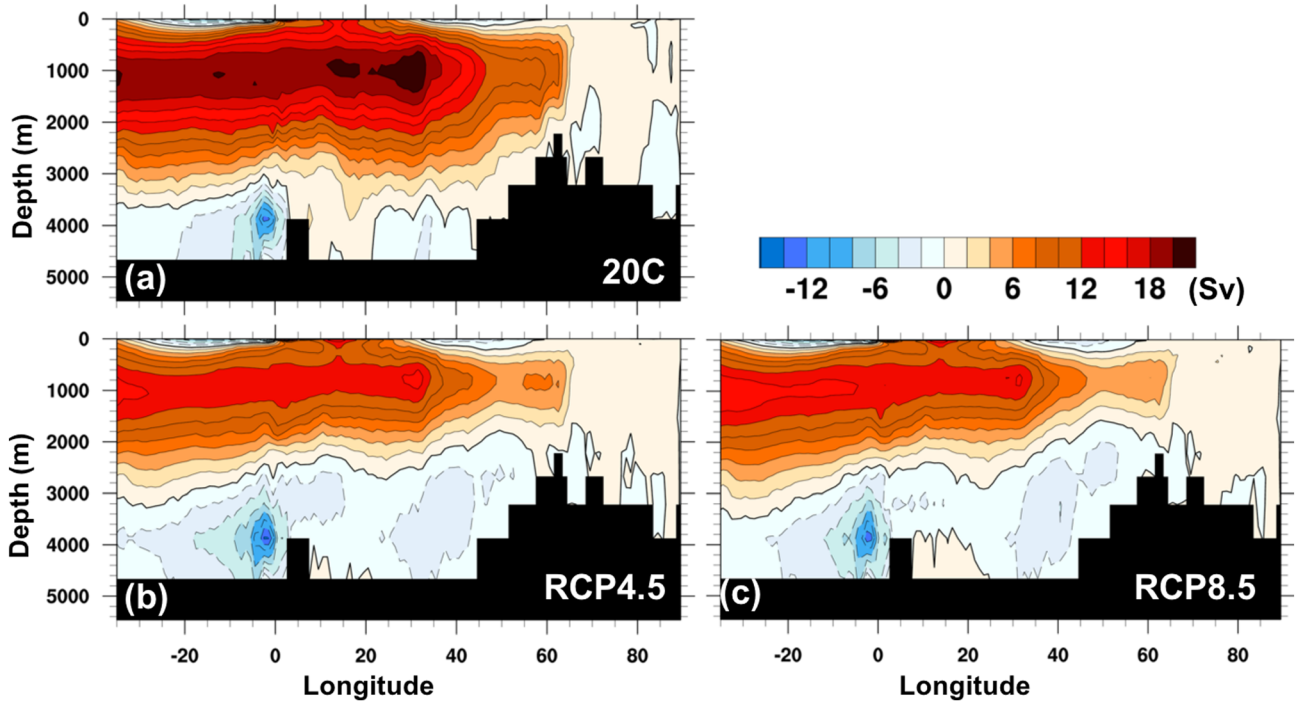

Figure 9. ROM mean 1976–2005 (a) and 2070–2099 (b, c) Atlantic meridional overturning circulation.

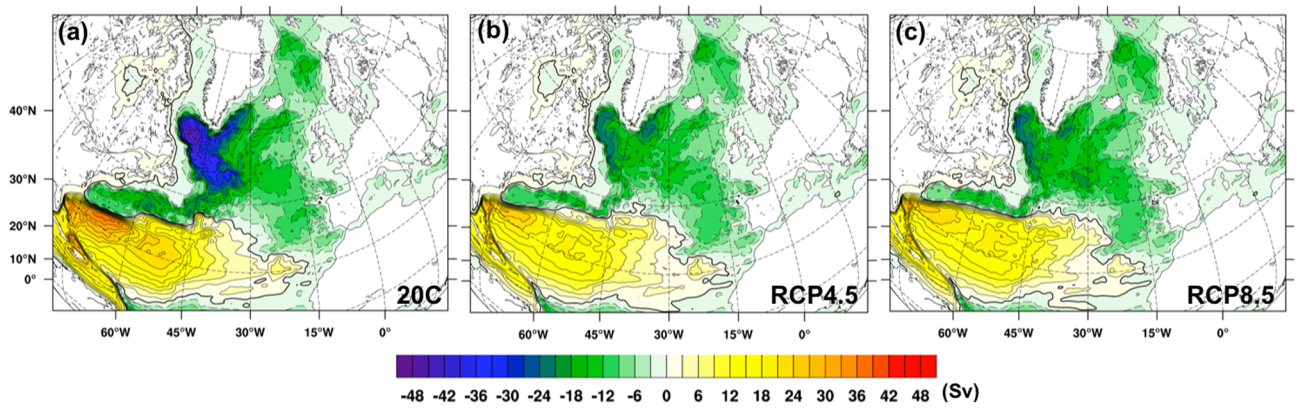

Figure 10. ROM mean 1976–2005 (a) and 2070–2099 (b, c) barotropic stream function.

as a zone of subdued warming, but 70% of the considered experiments featured an increase in SST, while the remaining 30% showed a reversed trend of which 15 cases were classified as "abrupt cooling." In their analysis, Sgubin et al. (2017) identified two main processes driving to an abrupt SPG cooling. The first one is driven by a local decrease in the mixed-layer thickness (convection collapse) without completely disrupting the AMOC; the second one is a generalized AMOC disruption.

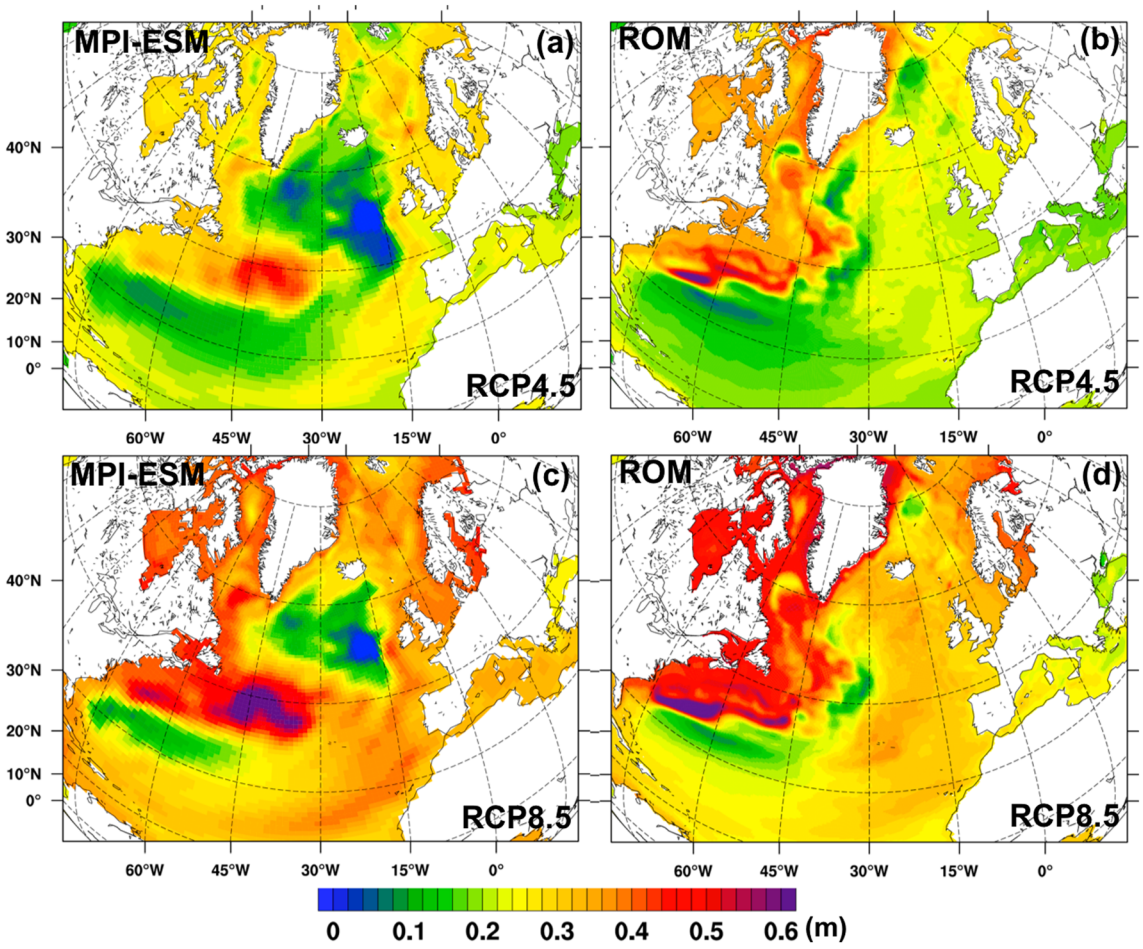

Figure 11. ROM mean sea level change (2070–2099 minus 1976–2005) including steric sea level rise.

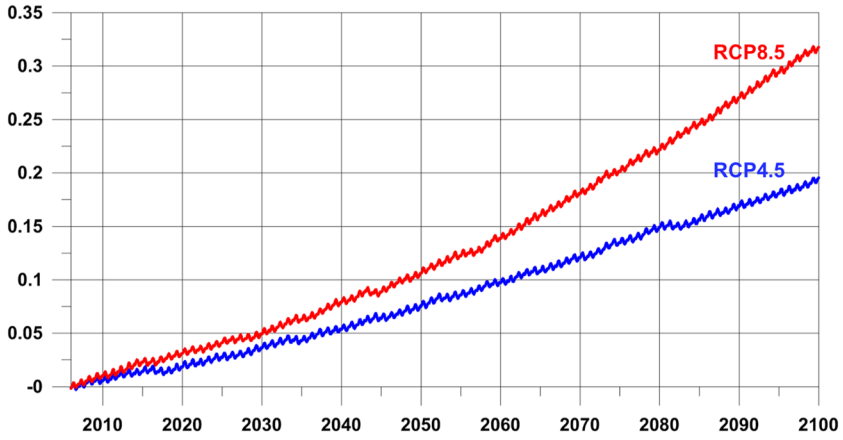

Figure 12. ROM global steric sea level change.

Interestingly, Sgubin et al. (2017) showed that the two CMIP5 configurations of MPI-ESM they analyzed do not present the abrupt cooling at SPG. On the other hand, ROM does it for RCP4.5 (Figure 8a). Figure 8 shows the time series of sea surface height (SSH) and mean S, T, and MLD in the upper 80 m, averaged over 37–53°W and 53–58°N along with the freshwater flux through the Denmark Strait. It can be seen that the cooling and freshening trend is accompanied by an increase in freshwater flow from the Denmark Strait and in the SSH (SPG index), and a reduction of the MLD. The freshening of the SPG may decrease the background stratification. Then, the SPG cyclonic circulation, partly driven by buoyancy forcing, weakens (see Figure 10), and the inflow of salty water from the subtropics is reduced (Hatun, 2005; Sgubin et al., 2017), which further amplifies the freshening and increases stratification. In RCP4.5 (Figure 8a), these feedback mechanisms further inhibit the local deep convection up to its permanent collapse, thus provoking a local abrupt cooling due to a drastically reduced MLD (Sgubin et al., 2017), while in RCP8.5 the MLD reduces more gradually (although with remarkable interannual variability; Figure 8b). Therefore, a strong SPG circulation favors deep convection, and a weaker SPG circulation will reduce deep water formation and generate a shallower MLD. This positive feedback leads to instabilities in the SPG system, which may switch from a strong circulation mode to a weak one (Sgubin et al., 2017).

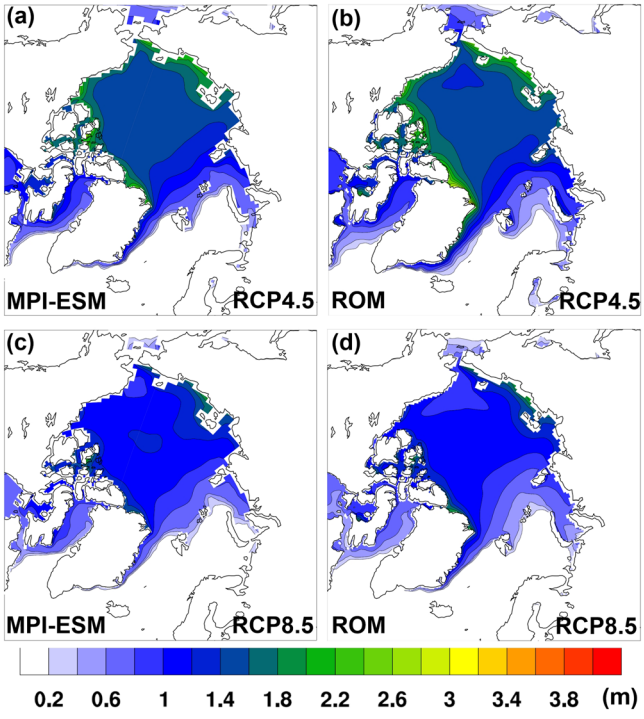

Figure 13. Mean 2070–2099 Arctic sea ice thickness in March as simulated by MPI-ESM (a, c) and ROM (b, d) for RCP4.5 (a, b) and RCP8.5 (c, d) scenarios.

In the ROM experiments performed with RCP4.5 and RCP8.5, AMOC is considerably reduced, but not disrupted (Figure 9). Hydrographic changes in the NA could result from a combination of warming with a weakening of the AMOC (Buckley & Marshall, 2016; Drijfhout et al., 2012). While it is beyond the purpose of this study to distinguish the quantitative contribution of these two processes, it is worth pointing out that Jackson et al. (2015) recently investigated the single effect of AMOC slowdown. Our results are consistent with many of the features described there. These include the effect of SPG freshening, the weakening of convection and, especially, a strong and widespread shallowing of the MLD in the NA.

Another effect of the slowdown of the AMOC is an extended cooling in the NA, as detailed in Jackson et al. (2015). While the cooling effect due to the weakening also occurs in our simulations, this is masked by a strong warming that occurs in response to climate change. In RCP4.5, the cooling effect is still seen as an extension of the SPG cooling, with a reduction of the overall ocean surface warming that can be even negative (Figure 6b). This warming is also seen in the

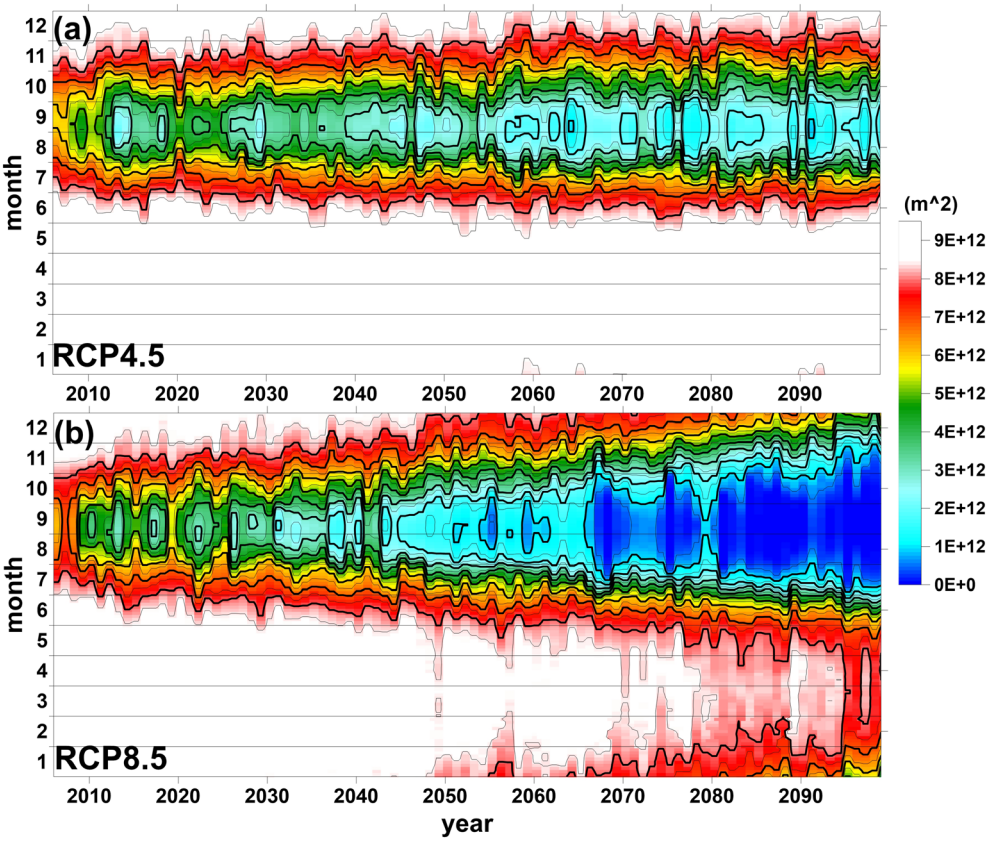

Figure 14. Arctic sea ice extent as simulated by ROM for RCP4.5 (a) and RCP8.5 (b) scenarios.

atmosphere (Figure 6f), being detectable as far as Western Europe. In contrast, in the high emission scenario (i.e., RCP8.5), the cooling has virtually vanished, and the effect of the down-slowed AMOC is almost offset by the stronger radiative forcing, resulting in a local damping of the warming (Figure 6g).

The different SPG response in MPI-ESM and ROM points to the importance of a higher resolution for properly representing the regional responses to global warming. In the ocean, vector properties (e.g., currents) show more spatial variation and gradients on small distances than scalar properties (e.g., temperature). Therefore, a proper representation of currents requires high-resolution models (e.g., Sein et al., 2018). On the other hand, properties like temperature, which are strongly influenced by air-sea interactions, can only be more realistically simulated with coupled ocean-atmosphere models (e.g., Gröger et al., 2015) in which high resolution in the atmosphere is desirable (e.g., Ma et al., 2016). Then, the higher resolution of the oceanic and atmospheric components allows for a better representation of the SPG dynamics.

The reduction of AMOC and the changes in the SPG circulation in ROM under both scenarios is associated with a pronounced increase in the mean sea level along the northeastern coast of North America (Figure 11), with spatial patterns and values that are in good agreement with previous model studies (Yin et al., 2009). The global steric sea level change depicted in Figure 12 for both RCP4.5 and RCP8.5 also matches previous reports (Jevrejeva et al., 2014; Yin et al., 2009). The rise in 2100 for RCP8.5 lies close to the mode of the range computed by Jevrejeva et al. (2014).

Figure 13 shows the spatial distribution of mean March SIT for the 2070–2099 period. Under the RCP4.5 scenario, the differences between MPI-ESM and ROM remain similar to those described in the evaluation section: ROM has more sea ice in the Barents Sea and off the east coast of Greenland as well as thicker sea ice to the north of the Canadian Archipelago. Under RCP8.5, the ice edge simulated by both models becomes much more similar, with ROM sea ice edge extending slightly more to the south.

In general, there are many more differences between scenarios than between models. Under RCP8.5, the March sea ice in the central parts of the Arctic Ocean is, on average, about half a meter thinner than

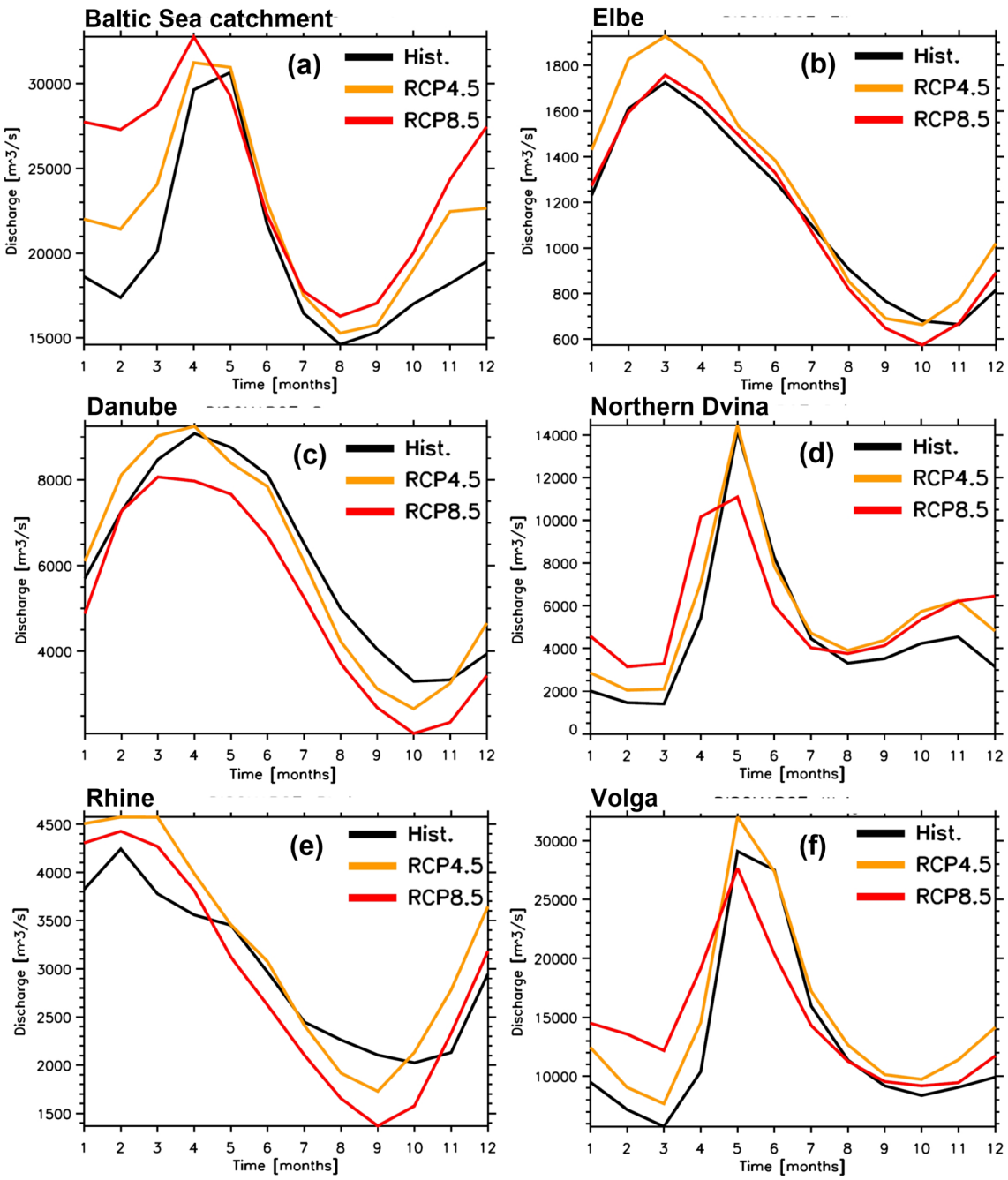

Figure 15. Simulated mean annual cycle of river discharge (m^3/s), historical (1976–2005), and RCP4.5 and RCP8.5 (2070-2099). (a) Baltic Sea catchment, (b) Elbe, (c) Danube, (d) Northern Dvina, (e) Rhine, and (f) Volga.

under RCP4.5. The evolution of the seasonal cycle of sea ice extent (SIE) in ROM under the two RCP scenarios is shown in the Hovmöller diagram of Figure 14, where the time evolution of the total SIE is represented. Under the RCP4.5 scenario, the trends in SIE are relatively small for most of the months except September. The melt season length only slightly increases, and the model never reaches the state with seasonally ice-free Arctic Ocean. The picture for RCP8.5 is completely different. Until about the year 2045 the seasonal cycle reminds that of RCP4.5, but then there is a strong decrease in SIE for all summer, fall, and winter months. The duration of the melting season gradually increases, and the system reaches its first seasonally ice-free state by the year 2055. By the end of the century the Arctic Ocean is ice free for 4 months a year.

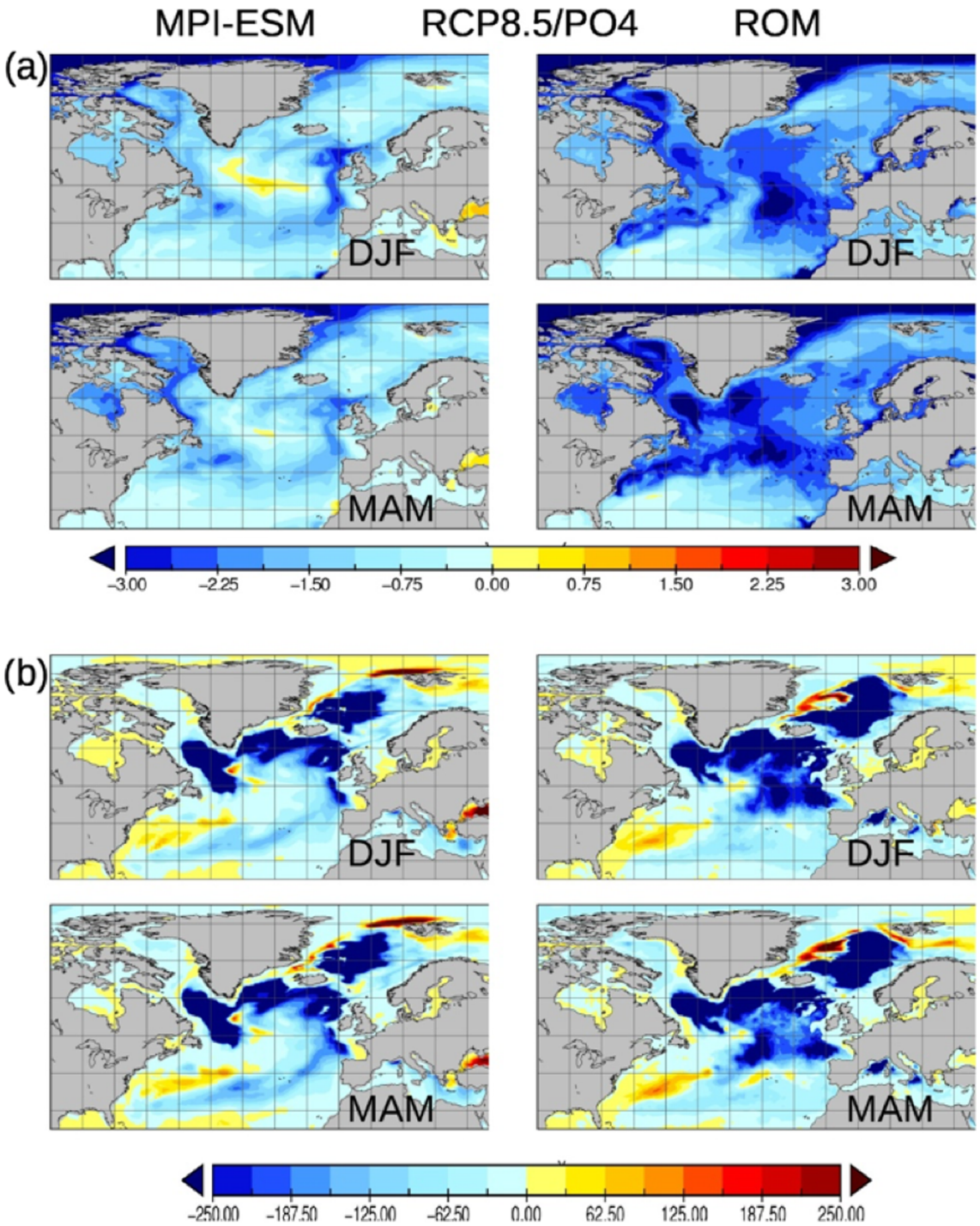

Figure 16. (a) Difference (2070–2099 minus 1976–2005) in dissolved phosphate near the surface (10^{-1} mmol/m^3). (b) Same as (a) but for mixed-layer thickness (m).

4.3. Hydrology

The projected discharges simulated by the HD hydrological model coupled to ROM are considered for a number of European catchments.

Future warming leads to an earlier snowmelt and a shift of precipitation from snow toward rain. This is seen in the projected discharge, where the snowmelt-induced discharge peak in spring is moved toward earlier

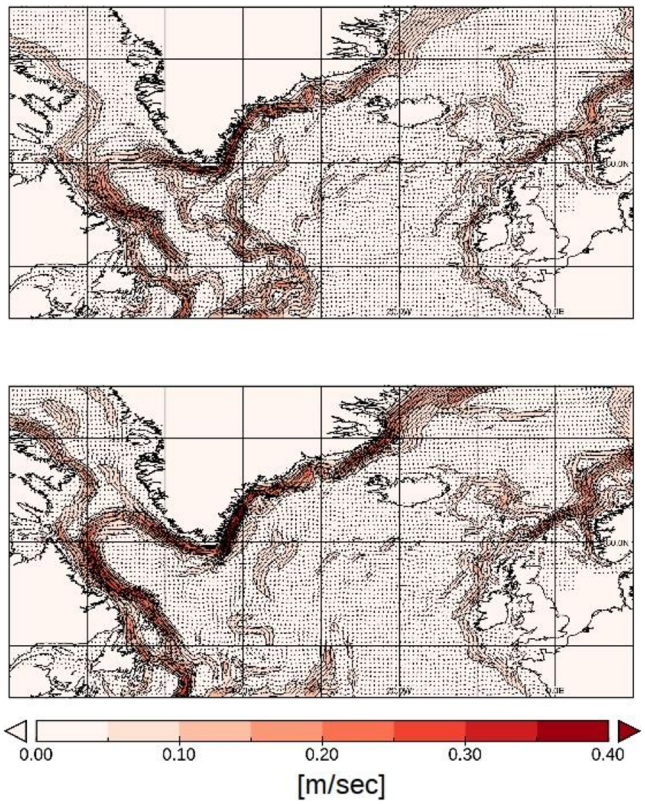

Figure 17. Circulation at 75 m depth for (a) 1976–2005 and (b) for RCP8.5 (2070–2099).

occurrence, especially for the Baltic Sea, Northern Dvina, and Volga (Figure 15). Future increases in precipitation, especially during the winter, lead to enhanced discharges during the winter for all catchments (except in the RCP8.5 scenario for the Danube) and even throughout most parts of the year for the Baltic Sea catchment, the Northern Dvina, and the Volga. Increases in precipitation are counteracted by rises in evapotranspiration (ET), especially during the summer. The latter leads to lower summer and autumn discharges than in the historical period for the Rhine and Elbe rivers. For the Danube, the ET increase is accompanied by a decrease of summer precipitation so that discharge becomes lower than in the historical period throughout almost the whole year except for RCP4.5 during winter. Generally, the climate change signals are larger in RCP8.5 than in RCP4.5. For the midlatitude rivers Elbe, Rhine, and Danube, the increase in ET and decreases in summer precipitation become more prominent than the increments in winter precipitation so that the RCP8.5 discharge is lower than for RCP4.5 throughout the whole year. Such a reduced RCP8.5 discharge also occurs for the Volga and the Northern Dvina in the second half of the year.

4.4. Biogeochemistry

Multimodel intercomparisons from the CMIP3 (Steinacher et al., 2010) and CMIP5 frameworks (Fu et al., 2016) give strong evidence that nutrient concentrations in the NA will decrease by the end of the 21st century. The depletion is strongest during winter and spring (Figure 16a). During the winter months, the nutrient anomaly pattern is controlled largely by physical changes such as the mixed-layer thickness (Figure 16b). The biological production is strongly limited by light, and chemical processes are slowed down due to lower water temperatures.

However, there are considerable differences between the two models. MPI-ESM shows a rather widespread and homogeneous nutrient reduction. Only along the NW European shelf edge, that is, from the northwestern corner of Spain to Scotland, the reduction is locally more pronounced. In contrast to this, much stronger nutrient reductions are predicted by ROM in nearly the entire NA (up to 35% in the midlatitude western NA) and the Arctic. The spatial pattern exhibits more small-scale structures than in the MPI-ESM case. Strong local reductions are seen in the Labrador Sea. In the southern part of the Labrador Sea the reduction is paralleled by weakened deep convection, which translates into a strongly reduced MLD (Figure 16b) and causes nutrient reductions there. The weaker convection is linked to a reduced salt transport to this area by southern waters originating from the Gulf Stream (Figure 17). This results in a less intense upward mixing of nutrient-rich deep waters, and so the outflow water of the Labrador Sea is likewise nutrient depleted. Part of this outflow water is directly injected into the Gulf Stream/NA drift, which, as a consequence, also shows reduced nutrient concentrations. Another part flows further southward along the north east American coast (Figure 16a). In the MPI-ESM model, the average ice edge in Greenland is shifted toward the east and north. This results in locally enhanced mixing near Spitsbergen (this is, in this location, greater in MPI-ESM than in ROM). This localized intensification of mixing in MPI-ESM damps the nutrient reduction north and west of Spitsbergen. This effect is also visible, but weaker, in ROM. The Arctic shows the most pronounced nutrient reduction. They are strongest during summer due to lower ice coverage, which leads to higher consumption of nutrients through enhanced primary production.

Despite the nutrient reductions during the cold season due to stronger stratification, changes in the yearly averaged primary production are rather low in both models. A positive effect on the yearly averaged productivity is, at first order, the prolonged season for phytoplankton to grow. Most areas show a slightly reduced production in the NA, whereas in the Arctic production is increased. Accordingly, we see strong changes in the seasonal timing of the bloom, as well as differences between the western and eastern NA. The main

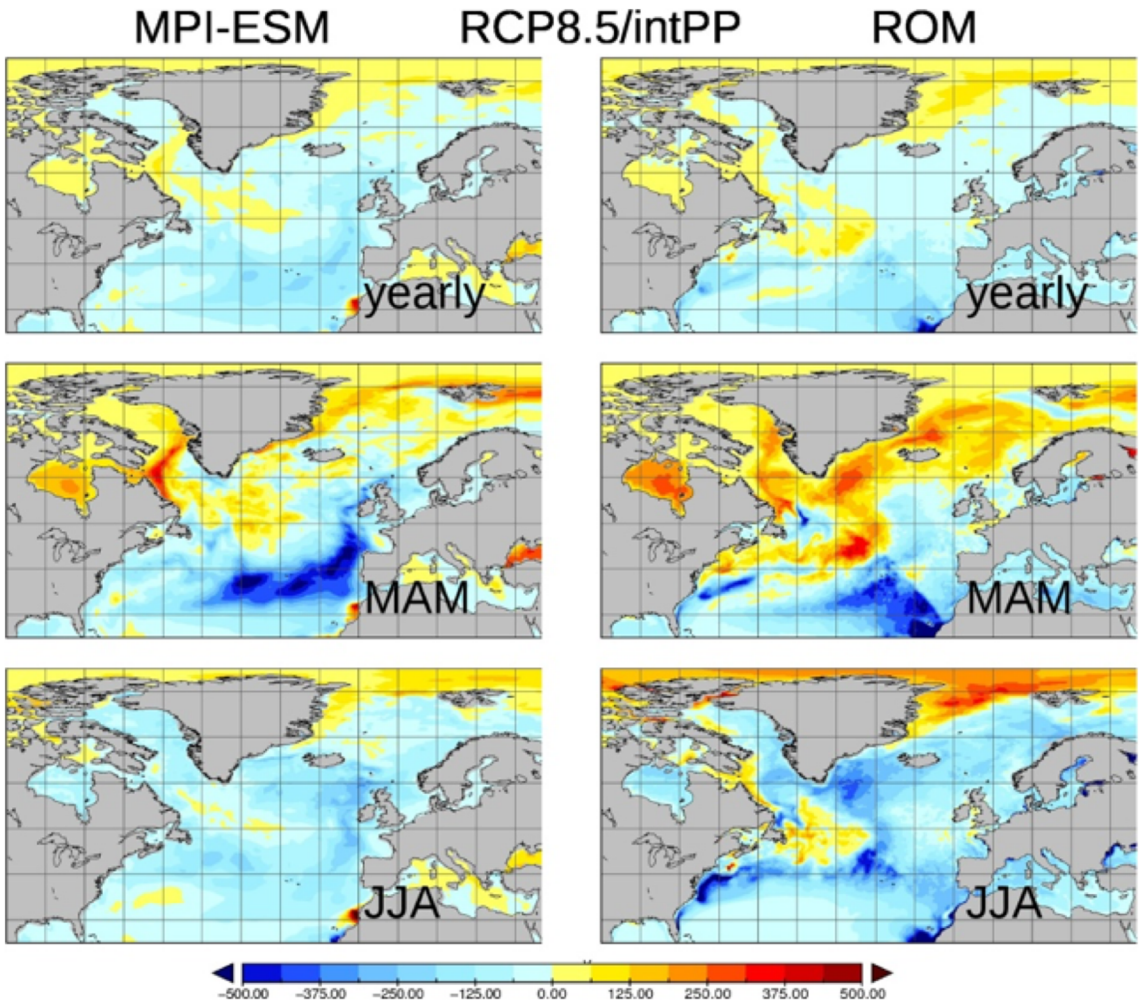

Figure 18. Difference (2070–2099 minus 1976–2005) in vertically integrated primary production (mgC/m^2/day).

reason is the earlier start of phytoplankton bloom resulting from the strong surface warming and the premature onset of thermal stratification. This effect is stronger in the western than in the eastern Atlantic because the western part is dominated by colder waters from the Arctic, which tend to delay the start of the bloom compared to the eastern Atlantic, which is occupied by warmer waters from the subtropics. Accordingly, the highest increase in spring productivity is seen along the flow path of the warmed East Greenland Current and the Labrador Current. In addition, the reduced sea ice coverage enhances the wind driven cyclonic circulation, and so the southward flow of nutrient rich Arctic waters within the East Greenland Current is also strengthened (Figure 17).

4.5. Impact on the NW European Shelf Seas

The NW European shelf seas have two external sources for nutrients, that is, riverine loads, as well as exchange with the adjacent NE Atlantic. The southwestern part of the NW European shelf, that is, the Bay of Biscay, has a relatively broad connection to the open ocean, and so the strong nutrient reduction during winter and spring seen in the NE Atlantic translates well onto the shelf. In this case, due to the well-established connection between the shelf and the ocean, nutrient concentration on the shelf becomes sensitive to nutrient changes in the open ocean. In contrast to this, the northern part, that is, the North Sea, is a marginal sea, which is surrounded by central Europe, Great Britain, and Norway. Indeed the North Sea is by far less affected than the Bay of Biscay and the NE Atlantic (Figure 18). This is true for both the MPI-ESM and ROM. Accordingly, the changes in total productivity in the North Sea are fairly moderate (Figure 18).

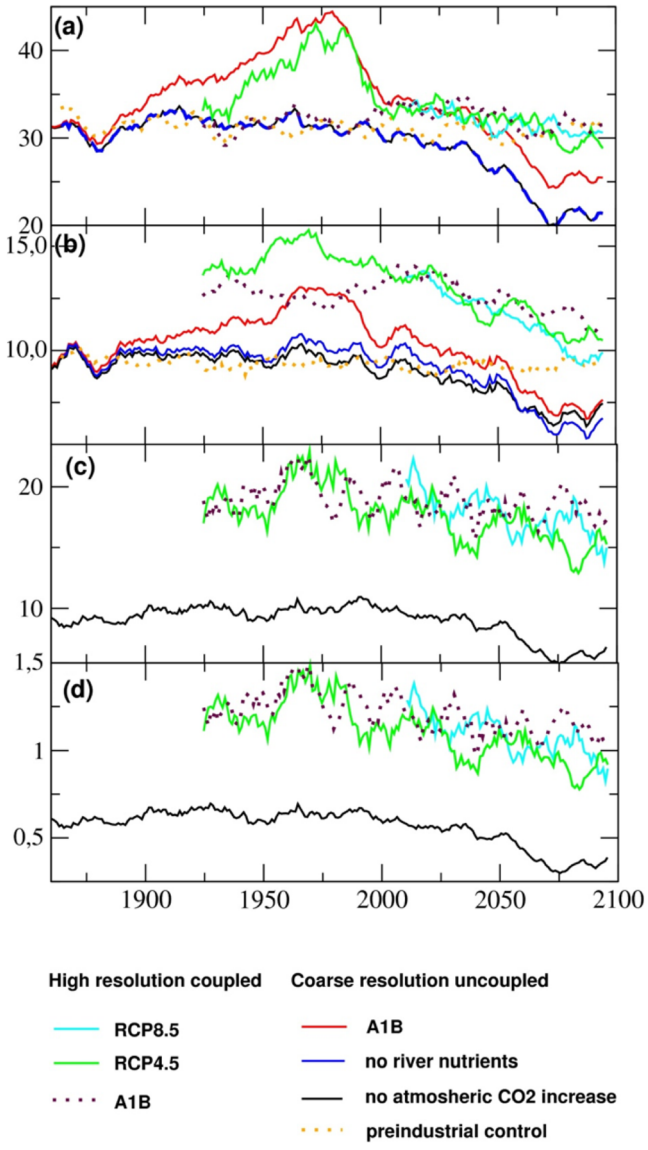

Figure 19. Area integrated biological parameters for the North Sea. (a) Simulated primary production (Mio.tC/a), (b) carbon dioxide absorption (Mio.tC/a), (c) transport of nitrate into the North Sea (kmol/s), and (d) transport of phosphate into the North Sea (kmol/s).

This result is somewhat surprising. A previous study (Gröger et al., 2013), using the same ocean and biogeochemistry model but in a somewhat coarser spatial resolution and with prescribed atmospheric forcing taken from MPI-ESM CMIP 3 model (Roeckner et al., 2006) following the A1B scenario, found a very strong impact on North Sea primary production at the end of the 21st century. It was caused by reduced nutrient transports from the NE Atlantic (Gröger et al., 2013). We therefore compare our results in the following to the simulation of Gröger et al. (2013) to investigate what the differences to this study are related to. Figures 19c and 19d compare the diagnosed nutrient transports from the NE Atlantic over the shelf edge into the North Sea for the different scenarios and model setups. The transports simulated by the uncoupled setup without interactive air-sea fluxes have comparably low variability. In the second half of the 21st century, on-shelf transports strongly decline by up to 50% at the end of the simulation, which causes a dramatic reduction in primary production (Figure 19a, red curve). Further analysis has shown that the reduced nutrient transports were not due to decreased water volume transport but, in fact, water masses entering the North Sea were depleted with nutrients due to stronger stratification and reduced winter mixing in the adjacent NE Atlantic (see Gröger et al., 2013, for details). We here argue that the use of an ocean-only model without interactive coupling to an atmosphere model is the main reason for the differences.

All the coupled simulations used here show an almost twice as high nutrient transport into the North Sea (mainly due to higher volume transports). They also exhibit higher variability compared to the uncoupled setup, independently from the considered warming scenario (A1B, RCP4.5, and RCP8.5; Figures 19c and 19d, black curves).

The enhanced variability of the coupled runs is likewise seen in the SSTs in the NA, as well as in the North Sea (not shown). It is a well-known phenomenon that interactive air-sea coupling increases SST variability by reducing air-sea heat fluxes. This has been termed "reduced thermal damping effect" (Bhatt et al., 1998); that is, as the atmosphere is enabled to adapt to SST anomalies, air-sea heat fluxes are decreased, and so the damping of SST anomalies reduces as well. As the temperature of halocline waters will certainly affect the stratification and, thus, upward mixing of nutrient rich waters from depth, this will also influence the lateral nutrient transport in the upper layers.

There is a slight decreasing trend throughout the 21st century, but this trend is by far lower than the internal variability, and so the nutrient input to the North Sea remains on a high level. Accordingly, primary production in the North Sea is quite stable throughout the 21st century (Figure 19a, light blue, green, and dotted brown curves).

So the question arises: Why do the coupled high-resolution simulations only show a very slight reduction of production in the course of the 21st century although they display a similar strong stratification in the NE Atlantic like the uncoupled simulation does (Figure 16b)? Gröger et al. (2013) found the region of the northeastern Rockall Trough important for the nutrient transport into the North Sea. This region is located upstream for waters either passing the North Sea to the north or entering it west of Scotland through the straits of Faire Isle and Pentland Firth. In our scenario RCP8.5 the mixed-layer thickness decreases from about 950–900 m to around 600–700 m whereas in the uncoupled A1B scenarios, it decreases from around 750 m to below 350 m. From this, one would already expect a substantially lower impact on nutrient

transports into the North Sea in the coupled simulation compared to the uncoupled simulation. We further speculate that there is a critical value for the MLD in the Rockall Trough to maintain a vigorous nutrient transport to the North Sea, which has obviously been crossed in the uncoupled model during the climate warming of the A1B scenario. Such a threshold for the shoaling MLD in the NA and lowered nutrient transports to the NW European shelf has been recently found in longer-term climate simulations (>100 years; Mathis et al., 2019). Unfortunately, with the available simulations, we cannot ultimately investigate the different sensitivity of the MLD in the two setups.

We have compared the 10 m wind field of the coupled setup with the 10 m wind field used to force the uncoupled model (not shown). Throughout the last 50 years of the 20th century, the regionalized winter winds were in most regions of the NE Atlantic stronger than those used to force the uncoupled version (in the Rockall Trough, by around 0.8 m/s on average). This might favor stronger wind-induced mixing in the ocean model. Higher wind speeds could result from a positive feedback loop, which actively operates only in the coupled model.

Winter storm events induce strong mixing in the water column, which brings warmer waters from depth to the surface. In turn, the warmer surface waters destabilize the very cold winter atmosphere, which feeds back positively on wind speeds and wind-induced mixing. In the uncoupled setup, the prescribed atmosphere does not see the increasing SSTs due to mixing, and so the positive feedback on wind velocity and vertical mixing is lacking. Of course, the prescribed winds in the uncoupled model were taken from the coupled CMIP3 climate model MPI-ESM (Roeckner et al., 2006). But the global model was run with a longer time step and a substantially lower spatial resolution, which tends to smooth the amplitude of wind velocity and, thus, of wind-induced mixing. The positive feedback loop is well known for the NA (e.g., Sura & Newman, 2008; Watanabe & Kimoto, 2000) and has also been described recently in a regional coupled ocean atmosphere model for the North Sea and Baltic Sea region (Gröger et al., 2015).

In addition to wind-induced mixing, tidal and internal-wave-induced mixing at the continental shelf edge, and at the topographic barrier built up by the Rockall Plateau, has an influence on the MLD. In the uncoupled version, the tidal amplitude was damped by the ocean's model time step of 32 min compared to a time step of only 12 min in the coupled model.

Modeling of surface tides is very sensitive to spatial resolution and time step, but also, the quality of the tidal solution depends on the accuracy of the bathymetry (Stammer et al., 2014). This is more critical for internal tides with wavelengths 100–140 and 40–80 km for the first and second mode, respectively (Li et al., 2015). Surface and internal tidal dynamics are of paramount importance in coastal areas and on the shelf, including the shelf break. There, boundaries, topographic irregularities, and stratification contribute to generate a panoply of phenomena modifying the transport of properties through enhanced mixing and changes in mean circulation due to tidally induced residual currents (Izquierdo & Mikolajewicz, 2019). Although MPIOM does not simulate all the aspects of tidal dynamics, when enough spatial resolution is given, it is able to properly simulate the surface tide and the internal tide (Li et al., 2015; Müller et al., 2012) and their impact on mixing and residual circulation (Izquierdo & Mikolajewicz, 2019). Internal tides stand as an important mechanism for mixing and transport through the shelf break (e.g., Hall et al., 2011; Nash et al., 2004); therefore, any step improving their representation in climate models will have a positive impact on the modeling of marine biogeochemical cycles.

Many works predict, in the NW European shelf, a substantial decline of nutrient transports from the open ocean onto the shelf (Bopp et al., 2013; Gröger et al., 2013; Holt et al., 2012, 2018). For instance, Holt et al. (2012) used a global A1B scenario to drive a regional, high-resolution coupled ocean-biogeochemistry model and found a 20% reduction of on-shelf nutrient transport in the North Sea (a major basin on the NW European shelf). However, most of these studies were carried out by stand-alone ocean models only, which lack capability to realistically simulate the above-mentioned positive feedback loop. Due to this shortcoming, these studies may overestimate the vulnerability of nutrient transport to the NW European shelf.

Like primary production, also, the carbon uptake in the North Sea (Figure 19b) is not affected so much in the coupled model version. The reduction in the coupled simulations shows rather a smooth decline toward the end of the 21st century. This reflects at first order the local increases in water temperature, which decrease the solubility of carbon dioxide in seawater. As the biologically driven carbon uptake (mainly during the spring

bloom and warm season) remains fairly stable, no drastic changes during the second half of the century are seen.

5. Conclusions

In this work we have evaluated how far the consideration of a regionally coupled model system with higher resolution can provide a better representation of the regional climate and determine more robust climate change projections. The main conclusions are as follows:

1. The regionally coupled model ROM is able to reduce the biases of the GCM MPI-ESM compared to the reanalysis. In particular, ROM can reproduce features of the NA/European region, which are not present in the driving MPI-ESM. These differences are attributed to the higher ocean resolution, the regional coupling, and the better representation of key physical processes, leading to a better representation of the oceanic and atmospheric circulation at regional scales.
2. Regarding the climate change signal for the 21st century following the RCP4.5 and RCP8.5 scenarios, the projections for MPI-ESM and ROM show a large qualitative agreement. However, several crucial differences are identified at the regional scale. For example, ROM shows reduced SSTs in the SPG, which are not present in MPI-ESM, and a seasonally ice-free state is reached earlier in ROM (by 2055). This shows the importance of the higher resolution and the coupled system for determining the regional responses to global warming trends.
3. The coupled ROM provides several advantages in terms of the biogeochemistry on the NW European shelf compared to the MPI-ESM model. These improvements combine the avoidance of imperfect lateral boundary formulations (compared to limited area models) and permit of high resolution typical for regional models due to the unstructured grid. In terms of the climate change signal, ROM simulates a stronger widespread decline in winter nutrient concentration in the NA compared to the MPI-ESM. Differences are identified also for other features; for example, the phytoplankton spring bloom in the North-Western Atlantic sets in earlier and in the Arctic, and the yearly primary production additionally is enhanced in the late 21st century.

The better representation of the regional climate under recent climate conditions with ROM is associated primarily with the coupling at high resolution, a better resolved orography and bathymetry, a relatively independent large-scale circulation, and to the integration of ocean tides (which is not implemented in MPI-ESM). These new elements are very relevant in shaping the simulated present-time regional climate by ROM, showing important differences with respect to MPI-ESM. ROM generally corrects the global model deviations in the atmospheric fields, especially over land, presenting a more realistic JJA atmospheric circulation, together with an overall colder air temperature and reduced precipitation biases over Europe. In the ocean, high resolution leads to a substantial reduction of the biases of SST and SSS in the NA, partially correcting the reduced meridional SST gradient in the northern NA present in MPI-ESM, although it changes the strong warm bias to a cold bias. The improved SSTs lead to a better simulation of the storm track location and blocking frequencies over the East Atlantic and Europe and the Arctic sea ice cover.

The above-mentioned improvements are also relevant to the simulated climate change signal, leading to a modification of the climate projected by MPI-ESM. For T2M, the climate change signal is weaker in RCP4.5 than in RCP8.5 for both ROM and MPI-ESM, and the stronger warming in RCP8.5 enhances the hydrological cycle over Eastern Europe up to 20–50%. The regionally coupled model reduces the amplitude of the warming substantially, with differences of about 1°C (in the order of 25%) in the projected warming of several parts of the domain. Many of these areas correspond to locations with complex orography, thus reflecting the influence of the high resolution on T2M. Over land, the pattern of precipitation change is similar in both models, with increases over North Europe in winter and drier conditions in summer across Europe south of 55°N. The enhanced resolution of ROM reveals features undetected by MPI-ESM, such as the drier conditions along the northern shores of Iberia. The RCP8.5 scenario leads to stronger changes in precipitation, with a pattern consistent with the reduced blocking frequency.

Regarding SST, both MPI-ESM and ROM project a general warming, which is larger in the Gulf Stream region, particularly in RCP8.5. Under RCP4.5, ROM modifies significantly the SST warming pattern shown by MPI-ESM. The most remarkable difference is found for the SPG, where ROM is up to 3 K colder, indicating a local convection collapse (Sgubin et al., 2017). This SST change pattern (cooling at SPG and warming in

the Gulf Stream region) is a fingerprint of an AMOC slowdown (Caesar et al., 2018). Also, due to a larger general warming in RCP8.5, the surface cooling simulated by ROM in the SPG almost vanishes and is replaced by a meridionally stretched area of nearly unchanged SST.

SSS changes for both MPI-ESM and ROM display similar spatial patterns under both RCP4.5 and RCP8.5 scenarios, but with more marked increases/decreases in ROM. This is particularly evident over the SPG and in the Eastern NA. The different SPG response in MPI-ESM and ROM indicates the importance of a higher ocean resolution and regional coupling for properly representing local details, which may be decisive for representing regional responses to the global warming trend. Regarding the sea-ice conditions by the end of the century, ROM shows a SIT pattern similar to that from MPI-ESM under RCP4.5 scenario, but with a southward extension of the ice cover. Both models never reach the state with seasonally ice-free Arctic Ocean in this scenario: the differences become important for RCP8.5, where the ROM sea ice is clearly thinner and reaches a seasonally ice-free state well before MPI-ESM, namely, by the year 2055.

The changes in biogeochemistry are marked by a strong reduction in surface nutrient concentrations by up to 35% at the end of the 21st century. They are linked to lower vertical mixing and, accordingly, to lower transport of nutrient-rich deep waters into the euphotic zone. These changes are much more pronounced in ROM compared to MPI-ESM, especially in the western NA and the Labrador Sea, where surface water freshens substantially. Variations in the yearly integrated primary production are rather low but feature strong changes in seasonality. In the western NA, the southward flowing cold and nutrient rich waters in the East Greenland Current are warmed much earlier in the year and cause the spring bloom likewise to occur earlier. In the Arctic, the retreating sea ice cover improves light conditions and leads to stronger productivity during summer. This effect is more pronounced in ROM than in MPI-ESM.

The strong lowering of nutrient transports (up to ~50%) from the northeast Atlantic to the NW European shelf detected in previous works is less pronounced in the present study. The most likely explanation for this fact is the different approach of Gröger et al. (2013), who applied an ocean-only model directly forced by GCM output. Wind velocities over the NA were lower and thus probably led to weaker wind-induced mixing. In addition, the tidal dynamics representation was less accurate due to coarser resolution and the larger time step used. That setup made the model of Gröger et al. (2013) more sensitive to hydrographic changes, which tend to increase water column stability.

In summary, ROM introduces a benefit to the historical climate simulation due to the combination of both high-resolution and ocean-atmosphere coupling. Moreover, ROM has the ability to reduce some of the GCM biases in the representation of the present climate conditions. ROM also seems to be well suited for high-resolution climate change studies, especially in regions where air-sea coupling plays an important role. In particular, we find that the climate change signal across Europe is sensitive to the use of the regionally coupled model, with a general decrease in the projected warming. Over the ocean, the climate change signal in the NA is strongly affected by both the ocean and atmospheric high resolution. At these resolutions, air-sea interactions exert a relevant influence in regions such as the Gulf Stream and the Labrador Sea. This confirms that ROM is a powerful model to estimate the regional impacts of climate change.

Data Availability Statement

The data used in the paper are available online (at https://swiftbrowser.dkrz.de/public/dkrz_035d8f6ff058403bb42f8302e6badfbc/SeinROM2/).

Appendix A

A.1 Validation of the Atmospheric Fields

In this subsection, the simulation of the present climate of the NA in terms of the atmospheric variables is evaluated. Mean sea level pressure (MSLP) is generally a good indicator for a realistic simulation of the large-scale circulation, as erroneous MSLP gradients induce an incorrect regional wind circulation (e.g., Hueging et al., 2013). This, in turn, influences the simulated precipitation and temperature fields and can also have a strong effect on ocean circulation. Figure A1 displays the MSLP fields for the boreal winter,

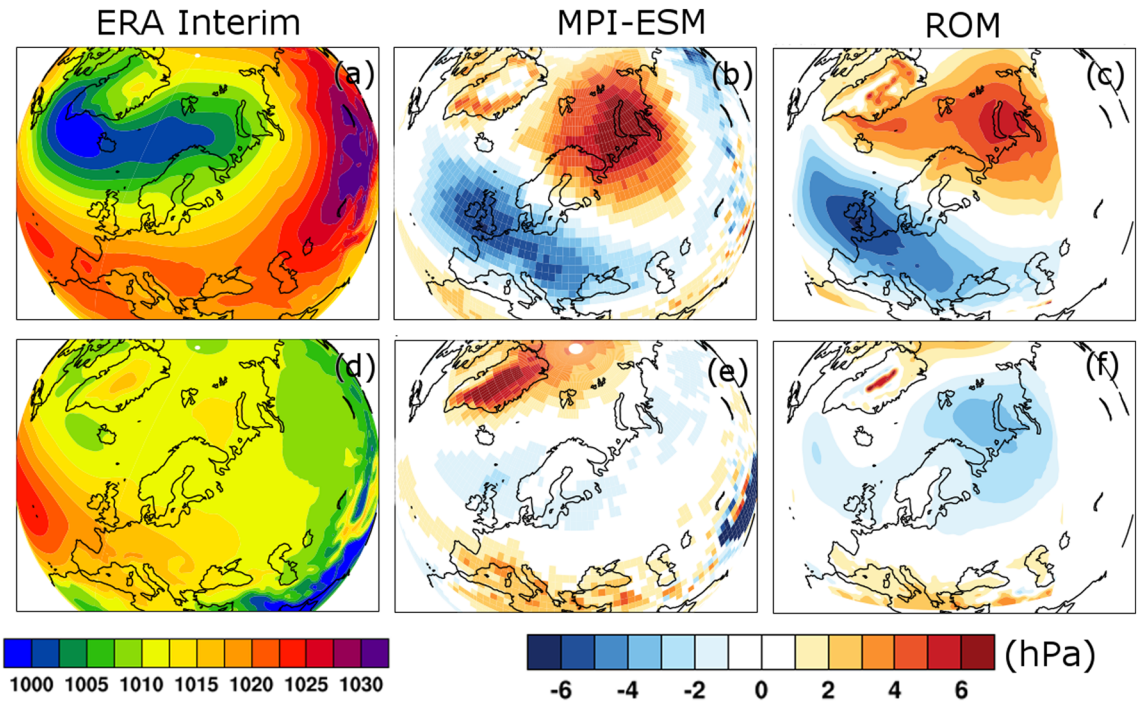

Figure A1. Mean sea level pressure for the 1976–2005 period for DJF (upper row) and JJA (lower row). (a and d) ERA-Interim and the differences Model Minus ERA-Interim: (b and e) MPI-ESM (c and f) ROM forced by MPI-ESM.

defined as December, January, and February (DJF), and summer, defined as June, July, and August (JJA). The values from ERA-Interim reanalysis (Dee et al., 2011) are used for comparison (Figures A1a and A1d).

The MSLP biases in these simulations are similar to those found with ROM forced by MPIOM/ECHAM5 (Sein et al., 2015). For DJF, a high-pressure anomaly is present at higher latitudes, extending from Greenland to Northern Russia and with maximum in the Kara Sea. Further south, a low-pressure anomaly with a maximum over the British Isles extends from the Labrador Sea to the Black Sea. These MSLP biases arise primarily from the MPI-ESM simulation (Figures A1b and A1c), but their magnitudes are modified by REMO: For example, the DJF positive MSLP anomaly in ROM is moderated over the Kara Sea and exacerbated along the eastern coast of Greenland. The DJF negative (up to −5 hPa) anomaly over the British Isles and Central Europe, already present in MPI-ESM, is slightly strengthened (for about 1 hPa) in ROM (Figures A1b and A1c). While the anomalies for JJA are weaker, ROM shows a negative MSLP anomaly over northern Scandinavia and the Kara Sea that is not present in MPI-ESM (cf. Figures A1e and A1f). These changes of MLSP imply a reduction of the meridional MSLP gradient in DJF and an enhanced north-south pressure gradient over continental Europe in JJA, thus leading to considerable changes in the near-surface winds. Sein et al. (2015) found similar biases with ROM forced by MPIOM/ECHAM5, but the biases are generally weaker for both the MPI-ESM and ROM forced by MPI-ESM.

Atmospheric large-scale circulation biases are further analyzed in more detail with the help of the storm track variability and blocking frequencies for both summer and winter. The storm track variability is quantified as the standard deviation of 500 hPa geopotential for a time window from 2 to 8 days. This variable is a rough quantification of the combined intensities and frequencies of low-pressure and high-pressure systems and thus of synoptic activity (e.g., Hoskins & Valdes, 1990). As for this frequency window the variability is dominated by low-pressure centers, the storm track intensity is primarily a measure for cyclone activity. The blocking frequencies are computed from 500 hPa geopotential height fields for reference latitude of 60°N following the approach of Tibaldi and Molteni (1990). For areas where the ROM data are not available, the corresponding information from ECHAM6 is used for the computations. Therefore, the MPI-ESM and ROM statistics are very similar except for the longitudes corresponding to the coupled model domain.

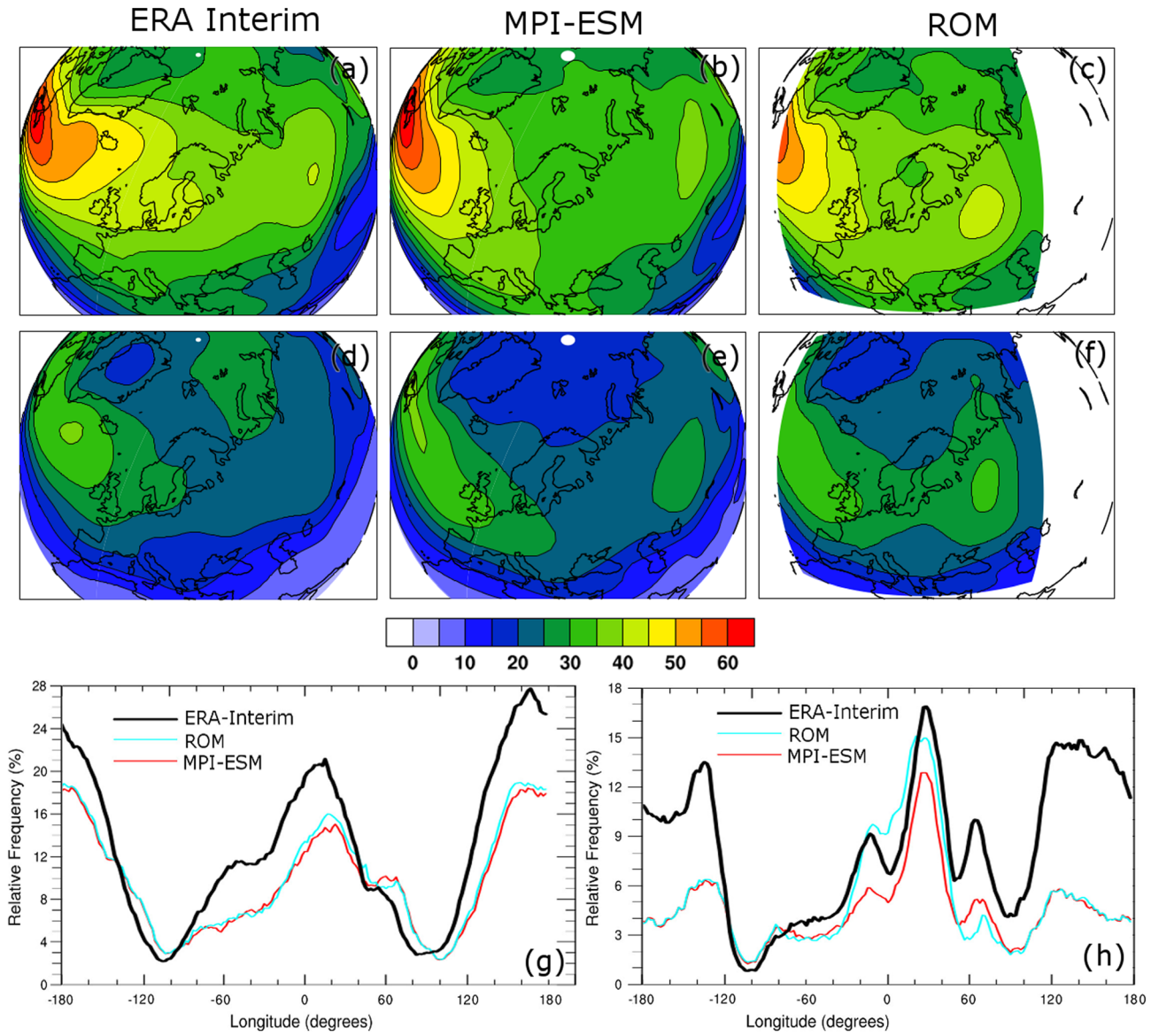

Figure A2. Standard deviation of DJF (1976–2005) band-pass filtered (2.5–7 days) 500 hPa geopotential. (a and d) ERA-Interim, (b and e) MPI-ESM, and (c and f) ROM forced by MPI-ESM. (g) Winter and (h) summer relative blocking frequency (after Tibaldi & Molteni, 1990) calculated on a daily basis. To calculate the blocking index, geopotential simulated by ROM was merged into the global geopotential field obtained from the corresponding driving model.

Storm track variability for ROM (Figures A2c and A2f) is generally weaker than in ERA-interim (Figures A2a and A2d). Over Europe, the storm track is displaced to the south, which is consistent with the southward-displaced MSLP gradient. These biases can also be found in MPI-ESM (Figures A2b and A2e) and are common to other GCMs (e.g., Ulbrich et al., 2008; Zappa, Shaffrey, & Hodges, 2013). ROM tends to show increased cyclone activity over continental Europe compared to MPI-ESM. This introduces an improvement in some areas and seasons, as Eastern Europe in winter, or South Scandinavia in summer, and an overestimation in other cases, most noticeably over Eastern Europe during summertime.

Figure A2g shows the DJF blocking frequencies for ERA-Interim, ROM, and MPI-ESM as a function of longitude. The blocking frequencies for both ROM (blue curve) and MPI-ESM (red curve) are somewhat reduced over the study area (60°W to 60°E) compared to ERA-Interim (black curve). Although both models show significantly lower blocking frequencies for this area, which is a common deviation in coupled models (Masato et al., 2013), blocking biases are slightly improved in ROM. This is in line with the above-described MSLP anomalies. For summer, the modeled blocking frequencies are closer to ERA-Interim for the study area

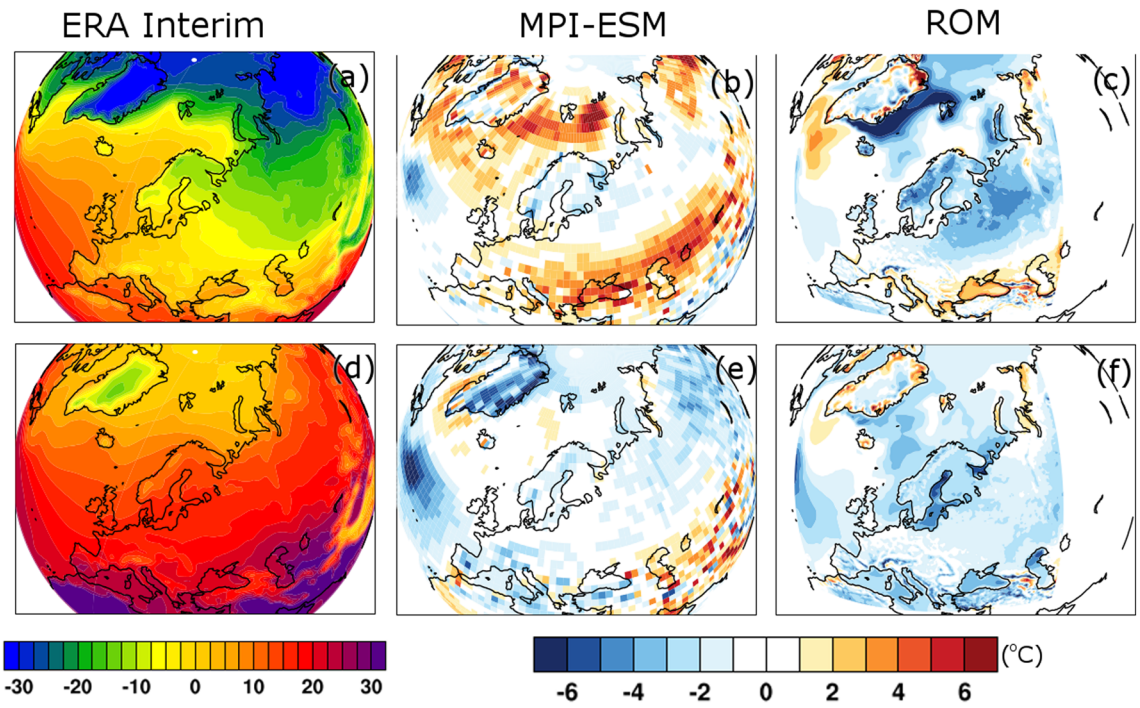

Figure A3. Mean 2-m air temperature for the 1976–2005 period for DJF (upper row) and JJA (lower row). ERA-Interim (a and d). The differences Model Minus ERA-Interim: MPI-ESM (b and e) and ROM forced by MPI-ESM (c and f).

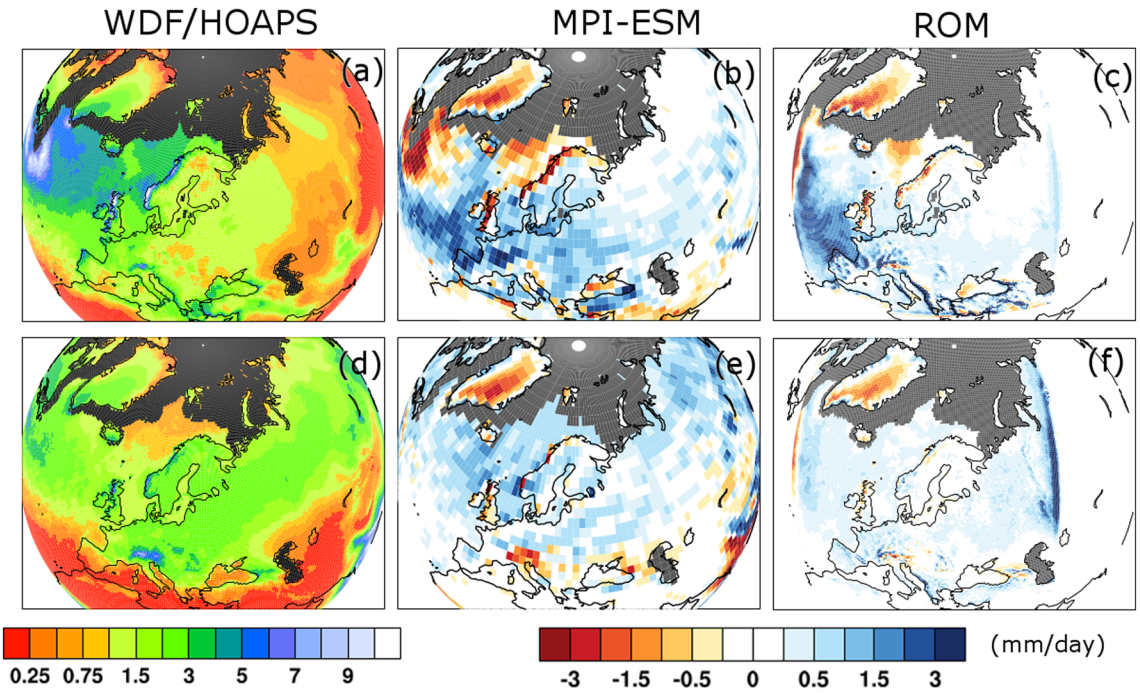

Figure A4. Mean precipitation obtained over land from WDF (Weedon et al., 2011) and over sea from HOAPS (Andersson et al., 2010) for the 1976–2005 period for DJF (a) and JJA (d). The differences Model Minus WFD/HOAPS: MPI-ESM (b and e) and ROM forced by MPI-ESM (c and f). Missing HOAPS data are colored with gray. Positive biases are indicated in blue and negative in red.

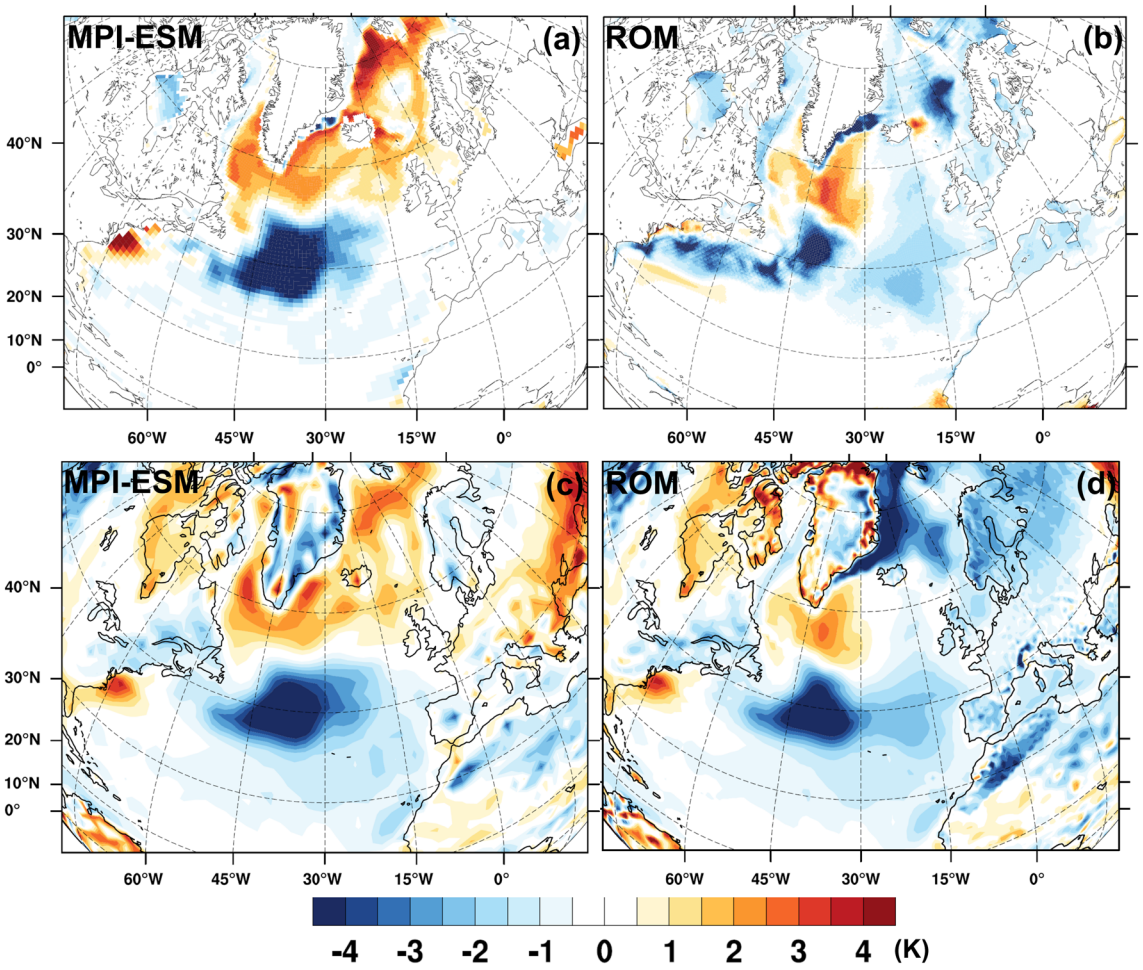

Figure A5. Mean (1976–2005) SST difference. MPI-ESM (a) and ROM (b). Model WOA09 climatology and mean 2-m temperature difference. MPI-ESM (c) and ROM (b). Model ERA-Interim. In (d) ROM results are merged into MPI-ESM.

(60°W to 60°E). Generally, MPI-ESM underestimates the frequency of blocking, while ROM partially compensates for the strong negative bias in MPI-ESM. In both cases, these results are in line with the above-described MSLP and winter storm track changes.

The biases in the simulated large-scale circulation described above have implications for regional climate, in particular for the near-surface (2 m) temperature (T2M). The DJF and JJA T2M biases with respect to ERA-Interim for both ROM and MPI-ESM are shown in Figure 4. The spatial patterns of these biases show strong differences: Generally, ROM simulates better the near-surface temperature in Central and Southern Europe, whereas MPI-ESM shows lesser T2M biases over northeastern Europe.

In winter, ROM shows significantly colder deviations than MPI-ESM (compare Figures A3b and A3c). The departures are typically below 3 K and lie over most of the coupled domain, and over Central and Southern Europe, within 2 K, except for the Alpine region and an area between the Caspian and the Black Sea. The stronger negative biases extend from Scandinavia into Russia (Figure A3c compared to Figure A3b), over areas likely snow covered in winter, possibly pointing to the need of improvements in the representation of land-atmosphere exchanges in the region. The T2M east of Greenland, from Iceland to Svalbard, and over the Barents Sea is strongly reduced, reversing the MPI-ESM warm bias over the Barents and Kara Seas area as well as east of Greenland over the ocean. The biases over Eastern Greenland are consistent with corresponding SIT biases (see section A.2 and Figure A7).

In summer, both ROM and MPI-ESM exhibit mostly cold biases over the domain (Figures A3e and A3f). This can be explained by the stronger north-south pressure gradient (Figures A1e and A1f), and the associated

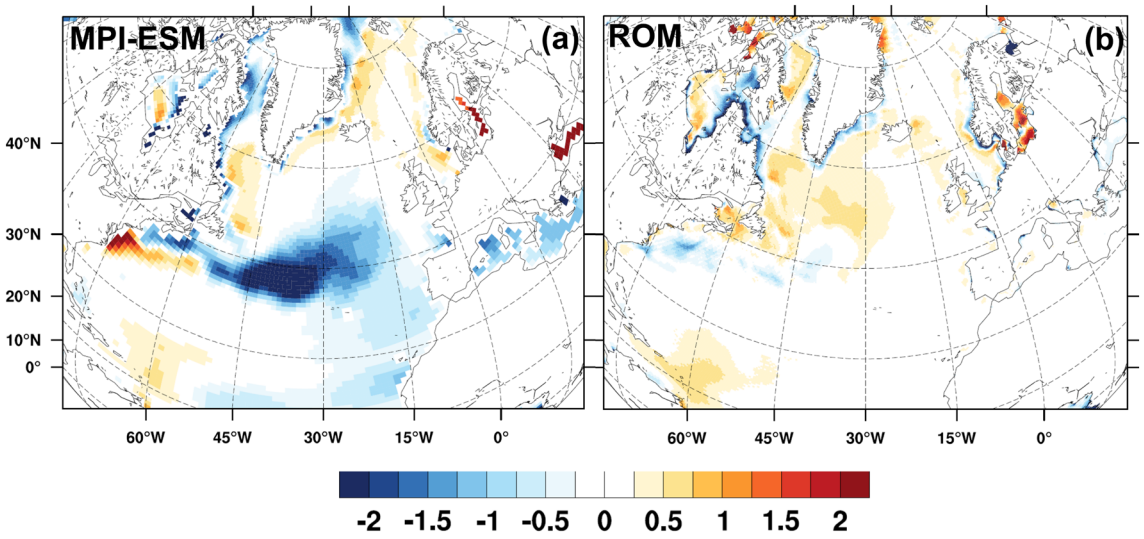

Figure A6. Mean (1976–2005) SSS difference. MPI-ESM (a) and ROM (b). Model WOA09 climatology.

anomalous westerly flow and stronger maritime influence, and by the reduced blocking frequencies over Eastern Europe, particularly for MPI-ESM (Figure A2h), provided that summer blocking events typically enhance T2M. In the case of ROM, the relatively high cyclone activity in summer over Eastern Europe (Figure A3f vs. Figure A3d) might play a role toward the cold bias in the area. The different sign of the bias over the northeastern NA is noteworthy: Values are slightly positive for MPI-ESM and of an opposite sign for

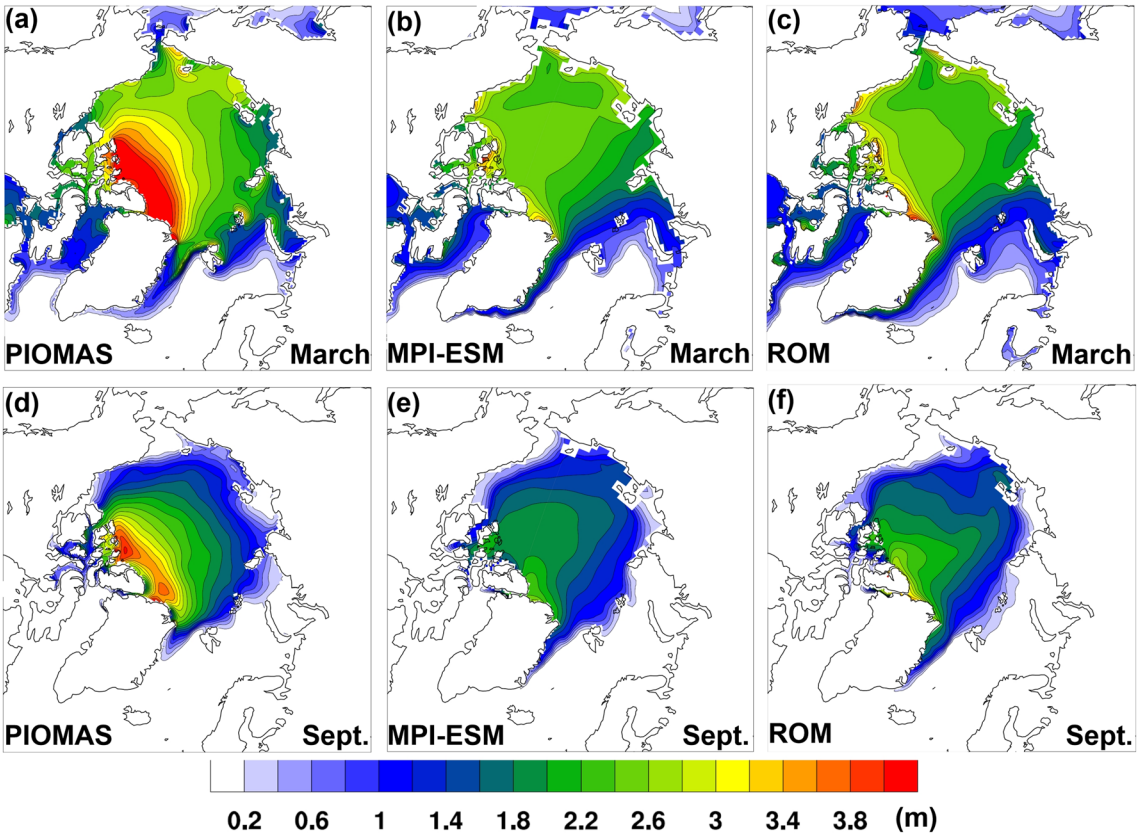

Figure A7. Mean (1976–2005) sea ice thickness.

ROM, which possibly arises from modifications in the ocean circulation due to the higher ocean model resolution. ROM shows stronger air and water temperature biases than MPI-ESM in the GIN seas, particularly in the East Greenland Current. This can be associated with the broader SIE in ROM. Differences over land, especially in mountainous regions, can be partially attributed to differences in topography resolution.

The simulated mean boreal winter and summer precipitation biases are shown in Figure A4. The global and the regional models show quite different behavior. ROM clearly shows better results in most of the common domain (except near the boundaries). The improvement of the precipitation biases by the regional model are clear over continental Europe, especially in regions with complex orography, whereas the improvement is less obvious over Greenland. Over the ocean, no clear improvements can be identified, except for the Labrador Sea.

A.2 Validation of the Ocean and Sea Ice Fields

In general, the simulated SST and SSS biases shown in Figures A5 and A6 for MPI-ESM and ROM are very similar to those obtained by Sein et al. (2015) for ECHAM5/MPIOM and ROM forced by ECHAM5, respectively. MPI-ESM SST presents a reduced meridional gradient in the northern NA compared to WOA09 climatology (Locarnini et al., 2010), with a strong positive bias to the north of the subpolar front and a strong negative bias to the south. This bipolar structure is somehow corrected in ROM, although it retains a strong cold bias between 40° and 60°W (Figure 6b) corresponding to a shift in the NA current (Sein et al., 2015). In the GIN seas the strong warm bias present in MPI-ESM corresponds to a cold bias in ROM. This difference is attributable to the change in ocean model resolution (Sein et al., 2015).

The SST anomalies over the NA have a strong influence on the large-scale atmospheric circulation, as the storm track location tends to be collocated with the areas of stronger meridional SST gradients due to the local maximum of low-level baroclinicity. The different blocking frequencies (see Figure A2) and the more extensive sea ice cover east of Greenland (Figure A7) could also be partially associated with these differences.

Compared to the WOA09 climatology (Antonov et al., 2010), MPI-ESM presents a strong fresh bias in SSS corresponding to the cold anomaly in SST (Figure A6a) and extending eastward to the European shelf. To the north, however, the SSS bias is very small. ROM shows almost no SSS bias in the NA, being only slightly saltier in the SPG area. In both cases SSS biases are much smaller than those obtained by Sein et al. (2015), which is probably caused by the stronger salinity surface restoring. Compared to simulations done in Sein et al. (2015), we increased the restoring constant. In terms of time, instead of 6 months, 3 months were used, which is still large enough compared to most stand-alone global ocean models.

The restoring was done as described in the following. First, one historical simulation (1920–2005) was done using salinity relaxation. Then, we obtained the climatological (1970–2000) virtual freshwater flux needed for this kind of restoring and used it for further simulations, but in the coupled area only. In general, we used two types of salinity restoring. In the coupled area, a monthly mean climatological freshwater flux correction was applied, whereas for the uncoupled ocean, we used salinity restoring in its traditional "stand-alone ocean" form, that is, relaxation to the Polar Science Center Hydrographic Climatology (PHC) (Steele et al., 2001) for the historical run. In the scenario simulations, the relaxation to PHC plus monthly-mean salinity anomalies obtained from MPI-ESM was used for the uncoupled ocean. In the coupled area, the restoring remained unchanged, that is, as a constant climatological flux correction. Additionally, salinity restoring (flux correction) was completely switched off under sea ice and in the North and Baltic seas. To avoid unrealistically strong restoring toward too high salinities in river mouths, restoring was switched off in regions where surface salinity was less than 28 by applying a smooth transition coefficient changing from 0 ($S < 28$) to 1 ($S > 30$) (see detailed description in Marsland et al., 2002, and Sein et al., 2015).

Figure A7 shows the spatial distribution of the SIT in MPI-ESM and ROM historical simulations as well as SIT fields from the PIOMAS. The latter is a reanalysis of the SIT and, due to the lack of any reliable long term climatology, is used here as a relatively good approximation of the real-world SIT distribution (J. Zhang & Rothrock, 2003).

Differences in SIT mean distribution between MPI-ESM and ROM, especially noticeable in September, might be partly explained by the fact that the boundary of the ROM model domain splits the Arctic Ocean in two halves approximately across the Lomonosov ridge (Figure 1). In September ROM produces thicker

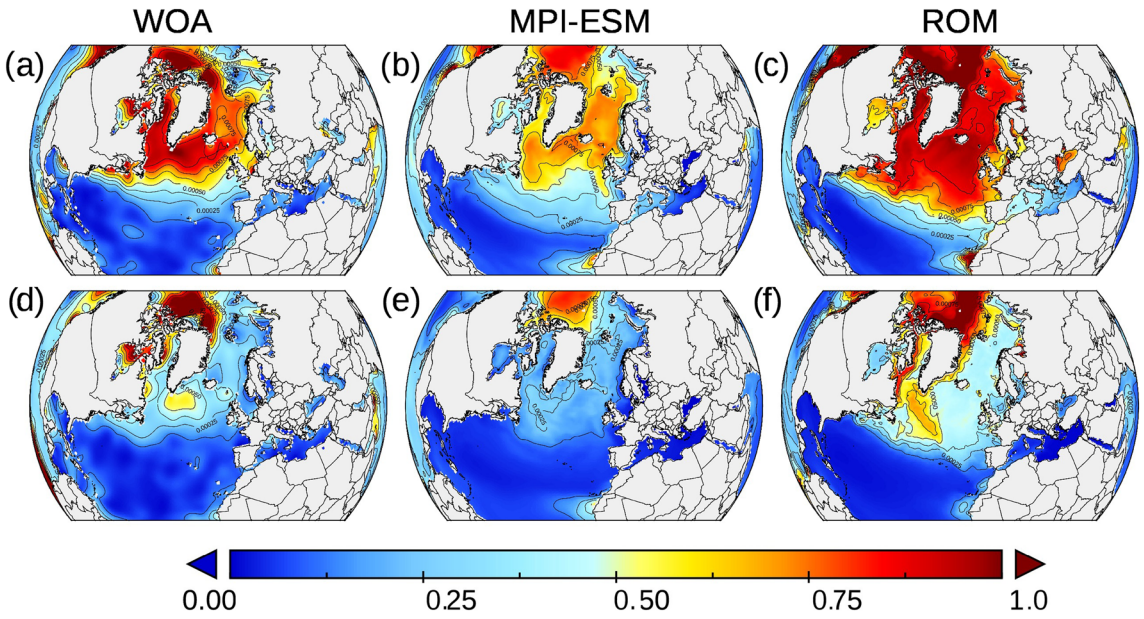

Figure A8. Mean (1976–2005) dissolved phosphate concentrations (mmol/m^3). WOA refers to the observational climatology from the World Ocean Atlas (Garcia et al., 2009).

ice in the Eurasian Basin of the Arctic Ocean compared to MPI-ESM, while in March ROM also has notably more sea ice along the Greenland shore and in the Barents Sea. Both MPI-ESM and ROM have on average thinner ice compared to PIOMAS reanalysis, especially to the north of the Canadian Archipelago. However, spatial distribution of March SIT over the central Arctic is slightly better in ROM with SIT more gradually decreasing toward the central part of the Arctic Ocean.

A.3 Validation of the Ocean Biogeochemistry

We here compare surface phosphate concentrations of the historical run with corresponding fields from the MPI-ESM historical run and observations from the World Ocean Atlas (Garcia et al., 2009). During winter a deep mixed layer and low productivity maintain overall high nutrient concentrations in the northern NA (Figure A8a). A steep gradient builds up around 40°N, as nutrient depleted surface waters from subtropical regions meet nutrient-rich water masses from the north, where nutrient consumption due to biological productivity remains low. These features are only insufficiently represented in MPI-ESM. Nutrient concentrations are, by far, too low in the entire NA (Figure A8b), and the pronounced north-south nutrient gradients around 40°N are not well reproduced. In contrast, these characteristics are much better represented in ROM although the transition between nutrient-rich northern waters and nutrient depleted

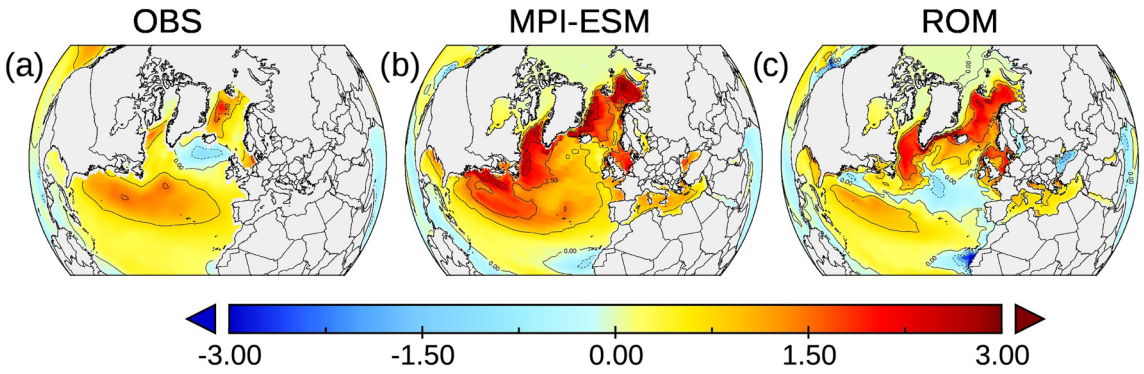

Figure A9. Air-sea carbon fluxes (10^{-9} kg m^{-2} s^{-1}). The observational data set OBS refers to Landschützer et al. (2017).

subtropical waters are a bit too far south. Both MPI-ESM and ROM overestimate nutrient concentrations at the NW edge of Africa. This is probably due to an overestimation of coastal upwelling there.

In summer, when biological productivity takes place and the mixed layer is shallower, most areas in the NA show reduced nutrient concentrations or are even nutrient depleted (Figure A8d). In MPI-ESM this nutrient reduction is strongly overestimated, while it is slightly underestimated in ROM. However, there are some local spots where high concentrations are seen, such as along the western margin of the Labrador Sea and at the southern tip of Greenland. These features are nearly completely absent in MPI-ESM, but they are clearly seen in ROM, although the spot south of Greenland extends too far east.

A.3.1 Carbon Fluxes

Figure A9 compares the winter air-sea carbon fluxes from the historical runs with MPI-ESM and ROM with an observation-based data set from Landschützer et al. (2017). During winter time, low water temperatures and a deepened mixed layer stimulate intense carbon uptake in the Nordic Seas. In the NA, a characteristic pattern with higher uptake east of northern Greenland and in a wide zone between ~35° to 45°N is observed (Figure A9a). In between, west of southern Greenland, carbon is transferred to the atmosphere. Although far from being perfect, ROM can substantially improve the spatial pattern of air-sea carbon fluxes compared to MPI-ESM. Especially, the area with carbon outgassing west of south Greenland is completely lacking in MPI-ESM. This feature is clearly seen in ROM, though it is a bit too far to the south and extends too far to the east. A spatial correlation between the modeled fluxes and the observational data set yields moderate correlation with ROM ($r = 0.50225$), but no correlation with MPI-ESM ($r = 0.0023243$). Thus, also, the carbon flux pattern benefits from regionalization with ROM. This is important, as the NA has been found to act as a major sink for the uptake of anthropogenic carbon dioxide (Sabine et al., 2004). Also here, in ROM and MPI-ESM, the NW edge of Africa shows too high carbon fluxes out of the ocean. This further points to an overall too strong upwelling in this area, which brings carbon (and nutrient) rich water masses to the surface.

Acknowledgments

The work of D. Sein was supported by the German Federal Ministry of Education and Research (BMBF) in the framework of the SODEEP project under Research Grant 01DJ18016B and the state assignment of the Ministry of Science and Higher Education of Russia (Theme 0149-2019-0015). N. Koldunov was supported by projects S1 of the Collaborative Research Centre TRR 181 "Energy Transfer in Atmosphere and Ocean" funded by the Deutsche Forschungsgemeinschaft (DFG, German Research Foundation)—Project 274762653. J. G. Pinto thanks the AXA Research Fund for support. W. Cabos thanks the CRYOPERU-CIENCIACTIVA 144-2015 project. The work of A. Dvornikov was supported by the grant of the Russian Foundation for Basic Research (RFBR) (Project 16-55-76021) and the state assignment of the Ministry of Science and Higher Education of Russia (Theme 0149-2019-0015). F. Álvarez-García and W. Cabos acknowledge the support of the Research Vice-Chancellorship of the University of Alcala through Project CCG2017/EXP-049. A. de la Vara was supported by the Spanish Ministry of Science, Innovation and Universities, the Spanish State Research Agency, and the European Regional Development Fund, through Grant CGL2017-89583-R. Simulations were performed at the German Climate Computing Center (DKRZ). We thank Marina Tarasova, the anonymous reviewers, and Andreas Oschlies for the constructive suggestions and critical remarks, which helped to improve the manuscript.

References

Andersson, A., Fennig, K., Klepp, C., Bakan, S., Graßl, H., & Schulz, J. (2010). The Hamburg Ocean atmosphere parameters and fluxes from satellite data—HOAPS-3. *Earth System Science Data*, *2*(2), 215–234. https://doi.org/10.5194/essd-2-215-2010

Antonov, J. I., Seidov, D., Boyer, T. P., Locarnini, R. A., Mishonov, A. V., Garcia, H. E., et al. (2010). In S. Levitus (Ed.), *World Ocean Atlas 2009, Volume 2: Salinity*, *NOAA Atlas NESDIS* (Vol. 69, p. 184). Washington, DC: U.S. Government Printing Office.

Behrenfeld, M. J. (2010). Abandoning Sverdrup's critical depth hypothesis on phytoplankton blooms. *Ecology*, *91*(4), 977–989. https://doi.org/10.1890/09-1207.1

Bopp, L., Resplandy, L., Orr, J. C., Doney, S. C., Dunne, J. P., Gehlen, M., et al. (2013). Multiple stressors of ocean ecosystems in the 21st century: Projections with CMIP5 models. *Biogeosciences*, *10*(10), 6225–6245. https://doi.org/10.5194/bg-10-6225-2013

Bozec, Y., Thomas, H., Elkalay, K., & de Baar, H. J. (2005). The continental shelf pump for CO2 in the North Sea—Evidence from summer observation. *Marine Chemistry*, *93*(2–4), 131–147. https://doi.org/10.1016/j.marchem.2004.07.006

Buckley, M. W., & Marshall, J. (2016). Observations, inferences, and mechanisms of Atlantic meridional overturning circulation variability: A review. *Reviews of Geophysics*, *54*, 5–63. https://doi.org/10.1002/2015RG000493

Bülow, K., Dietrich, C., Elizalde, A., Gröger, M., Heinrich, H., Hüttl-Kabus, S., et al. (2014). *Comparison of three regional coupled ocean atmosphere models for the North Sea under today's and future climate conditions*, *KLIWAS-27/2014* (p. 265). Koblenz, Germany: Koblenz, BfG. https://doi.org/10.5675/Kliwas_27/2014

Cabos, W., de la Vara, A., Álvarez-García, F. J., Sánchez, E., Sieck, K., Pérez-Sanz, J. I., et al. (2020). Impact of ocean-atmosphere coupling on regional climate: The Iberian Peninsula case. *Climate Dynamics*, *54*(9-10), 4441–4467. https://doi.org/10.1007/s00382-020-05238-x

Cabos, W., Sein, D. V., Durán-Quesada, A., Liguori, G., Koldunov, N., Martínez-López, B., et al. (2019). Dynamical downscaling of historical climate over CORDEX Central America domain with a regionally coupled atmosphere–ocean model. *Climate Dynamics*, *52*(7-8), 4305–4328. https://doi.org/10.1007/s00382-018-4381-2

Caesar, L., Rahmstorf, S., Robinson, A., Feulner, G., & Saba, V. S. (2018). Observed fingerprint of a weakening Atlantic Ocean overturning circulation. *Nature*, *556*(7700), 191–196. https://doi.org/10.1038/s41586-018-0006-5

Cai, W. J. (2011). Estuarine and coastal ocean carbon paradox: CO_2 sinks or sites of terrestrial carbon incineration? *Annual Review of Marine Science*, *3*(1), 123–145. https://doi.org/10.1146/annurev-marine-120709-142723

Collins, M., Minobe, S., Barreiro, M., Bordoni, S., Kaspi, Y., Kuwano-Yoshida, A., et al. (2018). Challenges and opportunities for improved understanding of regional climate dynamics. *Nature Climate Change*, *8*(2), 101–108. https://doi.org/10.1038/s41558-017-0059-8

Collins, M., Knutti, R., Arblaster, J., Dufresne, J.-L, Fichefet, T., Friedlingstein, P., et al. (2013). Long-term climate change: Projections, commitments and irreversibility. In T. F. Stocker, et al. (Eds.), *Climate Change 2013: The Physical Science Basis* (pp. 273–309). United Kingdom and New York, NY: Cambridge University Press. https://www.ipcc.ch/site/assets/uploads/2018/02/WG1AR5_Chapter12_FINAL.pdf

Dee, D. P., Uppala, S. M., Simmons, A. J., Berrisford, P., Poli, P., Kobayashi, S., et al. (2011). The ERA-Interim reanalysis: configuration and performance of the data assimilation system. *Quarterly Journal of the Royal Meteorological Society*, *137*(656), 553–597. https://doi.org/10.1002/qj.828

Drijfhout, S., Van Oldenborgh, G. J., & Cimatoribus, A. (2012). Is a decline of AMOC causing the warming hole above the North Atlantic in observed and modeled warming patterns? *Journal of Climacteric*, *25*(24), 8373–8379.

Fu, W., Randerson, J. T., & Moore, J. K. (2016). Climate change impacts on net primary production (NPP) and export production (EP) regulated by increasing stratification and phytoplankton community structure in the CMIP5 models. *Biogeosciences*, *13*, 5151–5170. https://doi.org/10.5194/bg-13-5151-2016

Garcia, H. E., Locarnini, R. A., Boyer, T. P., Antonov, J. I., Zweng, M. M., Baranova, O. K., & Johnson, D. R. (2009). *WORLD OCEAN ATLAS 2009, Nutrients (phosphate, nitrate, silicate)* (Vol. 4, NOAA Atlas NESDIS 71). Washington, DC: U.S. Government Printing Office. http://www.nodc.noaa.gov/OC5/indprod.html

Gröger, M., Arneborg, L., Dieterich, C., Höglund, A., & Meier, H. E. M. (2019). Summer hydrographic changes in the Baltic Sea, Kattegat and Skagerrak projected in an ensemble of climate scenarios downscaled with a coupled regional ocean–sea ice–atmosphere model. *Climate Dynamics*, *53*(9-10), 5945–5966. https://doi.org/10.1007/s00382-019-04908-9

Gröger, M., Dieterich, C., Meier, M. H., & Schimanke, S. (2015). Thermal air-sea coupling in hindcast simulations for the North Sea and Baltic Sea on the NW European shelf. *Tellus A: Dynamic Meteorology and Oceanography*, *67*, 26911. https://doi.org/10.3402/tellusa.v67.26911

Gröger, M., Maier-Reimer, E., Mikolajewicz, U., Moll, A., & Sein, D. (2013). NW European shelf under climate warming: Implications for open ocean-shelf exchange, primary production, and carbon absorption. *Biogeosciences*, *10*(6), 3767–3792. https://doi.org/10.5194/bg-10-3767-2013

Hall, R. A., Huthnance, J. M., & Williams, R. G. (2011). Internal tides, nonlinear internal wave trains, and mixing in the Faroe-Shetland Channel. *Journal of Geophysical Research*, *116*(C3), C03008. https://doi.org/10.1029/2010JC006213

Hatun, H. (2005). Influence of the Atlantic Subpolar Gyre on the Thermohaline Circulation. *Science*, *309*(5742), 1841–1844. https://doi.org/10.1126/science.1114777

Hewitt, H. T., Bell, M. J., Chassignet, E. P., Czaja, A., Ferreira, D., Griffies, S. M., et al. (2017). Will high-resolution global ocean models benefit coupled predictions on short-range to climate timescales? *Ocean Modelling*, *120*, 120–136. https://doi.org/10.1016/j.ocemod.2017.11.002

Hirschi, J. J.-M., Barnier, B., Böning, C., Biastoch, A., Blaker, A. T., Coward, A., et al. (2020). The Atlantic meridional overturning circulation in high- resolution models. *Journal of Geophysical Research: Oceans*, *125*, e2019JC015522. https://doi.org/10.1029/2019JC01552

Holt, J., Butenschon, M., Wakelin, S. L., Artioli, Y., & Allen, J. I. (2012). Oceanic controls on the primary production of the northwest European continental shelf: Model experiments under recent past conditions and a potential future scenario. *Biogeosciences*, *9*(1), 97–117. https://doi.org/10.5194/bg-9-97-2012

Holt, J., Polton, J., Huthnance, J., Wakelin, S., O'Dea, E., Harle, J., et al. (2018). Climate-driven change in the North Atlantic and Arctic Oceans can greatly reduce the circulation of the North Sea. *Geophysical Research Letters*, *45*, 11,827–11,836. https://doi.org/10.1029/2018GL078878

Holt, J., Wakelin, S., & Huthnance, J. (2009). Down-welling circulation of the northwest European continental shelf: A driving mechanism for the continental shelf carbon pump. *Geophysical Research Letters*, *36*, L14602. https://doi.org/10.1029/2009GL038997

Hoskins, B. J., & Valdes, P. J. (1990). On the Existence of Storm-Tracks. *Journal of the Atmospheric Sciences*, *47*(15), 1854–1864. https://doi.org/10.1175/1520-0469(1990)047<1854:oteost>2.0.co;2

Hueging, H., Haas, R., Born, K., Jacob, D., & Pinto, J. G. (2013). Regional Changes in Wind Energy Potential over Europe Using Regional Climate Model Ensemble Projections. *Journal of Applied Meteorology and Climatology*, *52*(4), 903–917. https://doi.org/10.1175/jamc-d-12-086.1

Hurrell, J., Kushnir, Y., Ottersen, G., & Visbeck, M. (2003). *The North Atlantic Oscillation: Climatic significance and environmental impact* (Vol. 134). Washington, DC: American Geophysical Union. https://doi.org/10.1029/GM134

Izquierdo, A., & Mikolajewicz, U. (2019). The role of tides in the spreading of Mediterranean Outflow waters along the southwestern Iberian margin. *Ocean Modelling*, *133*, 27–43. https://doi.org/10.1016/j.ocemod.2018.08.003

Jackson, L. C., Kahana, R., Graham, T., Ringer, M. A., Woollings, T., Mecking, J. V., & Wood, R. A. (2015). Global and European climate impacts of a slowdown of the AMOC in a high resolution GCM. *Climate Dynamics*, *45*(11-12), 3299–3316. https://doi.org/10.1007/s00382-015-2540-2

Jacob, D. (2001). A note to the simulation of the annual and inter-annual variability of the water budget over the Baltic Sea drainage basin. *Meteorology and Atmospheric Physics*, *77*(1–4), 61–73. https://doi.org/10.1007/s007030170017

Jevrejeva, S., Grinsted, A., & Moore, J. C. (2014). Upper limit for sea level projections by 2100. *Environmental Research Letters*, *9*, 104008. https://doi.org/10.1088/1748-9326/9/10/104008

Jung, T., Miller, M. J., Palmer, T. N., Towers, P., Wedi, N., Achuthavarier, D., et al. (2012). High-Resolution Global Climate Simulations with the ECMWF Model in Project Athena: Experimental Design, Model Climate, and Seasonal Forecast Skill. *Journal of Climate*, *25*(9), 3155–3172. https://doi.org/10.1175/jcli-d-11-00265.1

Jungclaus, J. H., Keenlyside, N., Botzet, M., Haak, H., Luo, J.-J., Latif, M., et al. (2006). Ocean Circulation and Tropical Variability in the Coupled Model ECHAM5/MPI-OM. *Journal of Climate*, *19*(16), 3952–3972. https://doi.org/10.1175/jcli3827.1

Landschützer, P., Gruber, N., & Bakker, D.C.E. (2017). An updated observation-based global monthly gridded sea surface pCO_2 and air-sea CO_2 flux product from 1982 through 2015 and its monthly climatology (NCEI Accession 0160558). Version 2.2. NOAA National Centers for Environmental Information. Dataset. [2017-07-11]

Laruelle, G. G., Cai, W. J., Hu, X., Gruber, N., Mackenzie, F. T., & Regnier, P. (2018). Continental shelves as a variable but increasing global sink for atmospheric carbon dioxide. *Nature Communications*, *9*(1), 454–454. https://doi.org/10.1038/s41467-017-02738-z

Li, Z., Von Storch, J.-S., & Müller, M. (2015). The M2 internal tide simulated by a 1/10° OGCM. *Journal of Physical Oceanography*, *45*(12), 3119–3135. https://doi.org/10.1175/JPO-D-14-0228.1

Limareva, N., Cabos, W., Izquierdo, A., & Sein, D. (2017). The climate change of the Caucasus as a result of the global warming. *Sovremennaya Nauka i Innovacii*, *2*(18), 19–32. ISSN 2307-910X

Locarnini, R. A., Mishonov, A. V., Antonov, J. I., Boyer, T. P., Garcia, H. E., Baranova, O. K., et al. (2010). In S. Levitus (Ed.), *World Ocean Atlas 2009, Volume 1: Temperature*, *NOAA Atlas NESDIS* (Vol. 68, p. 184). Washington, DC: U.S. Government Printing Office.

Ma, X., Jing, Z., Chang, P., Liu, X., Montuoro, R., Small, R. J., et al. (2016). Western boundary currents regulated by interaction between ocean eddies and the atmosphere. *Nature*, *535*(7613), 533–537. https://doi.org/10.1038/nature18640

Mahadevan, A., D'Asaro, E., Lee, C., & Perry, M. J. (2012). Eddy-driven stratification initiates North Atlantic spring phytoplankton blooms. *Science*, *337*(6090), 54–58. https://doi.org/10.1126/science.1218740

Marotzke, J., Müller, W. A., Vamborg, F. S., Becker, P., Cubasch, U., Feldmann, H., et al. (2016). MiKlip: A national research project on decadal climate prediction. *Bulletin of the American Meteorological Society*, *97*(12), 2379–2394. https://doi.org/10.1175/BAMS-D-15-00184.1

Marsland, S. J., Haak, H., Jungclaus, J. H., Latif, M., & Röske, F. (2002). The Max-Planck-Institute global ocean/sea ice model with orthogonal curvilinear coordinates. *Ocean Modelling*, *5*(2), 91–127.

Masato, G., Hoskins, B. J., & Woollings, T. (2013). Winter and summer Northern Hemisphere blocking in CMIP5 models. *Journal of Climate*, *26*(18), 7044–7059. https://doi.org/10.1175/JCLI-D-12-00466.1

Mathis, M., Elizalede, A., & Mikolajewicz, U. (2019). The future regime of Atlantic nutrient supply to the Northwest European Shelf. *Journal of Marine Systems*, *189*, 98–115. https://doi.org/10.1016/j.jmarsys.2018.10.002

Monerie, P.-A., Robson, J., Dong, B., Hodson, D. L. R., & Klingaman, N. P. (2019). Effect of the Atlantic multidecadal variability on the global monsoon. *Geophysical Research Letters*, *46*, 1765–1775. https://doi.org/10.1029/2018GL080903

Moore, G. W. K., & Renfrew, I. A. (2012). Cold European winters: Interplay between the NAO and the East Atlantic mode. *Atmospheric Science Letters*, *13*(1), 1–8. https://doi.org/10.1002/asl.356

Müller, W. A., Baehr, J., Haak, H., Jungclaus, J. H., Kröger, J., Matei, D., et al. (2012). Forecast skill of multi-year seasonal means in the decadal prediction system of the Max Planck Institute for Meteorology. *Geophysical Research Letters*, *39*, L22707. https://doi.org/10.1029/2012GL053326

Nash, J. D., Kunze, E., Toole, J. M., & Schmitt, R. W. (2004). Internal tide reflection and turbulent mixing on the continental slope. *Journal of Physical Oceanography*, *34*(5), 1117–1134. https://doi.org/10.1175/1520-0485(2004)034<1117:ITRATM>2.0.CO;2

Orr, J. C., Fabry, V. J., Aumont, O., Bopp, L., Doney, S. C., Feely, R. A., et al. (2005). Anthropogenic ocean acidification over the twenty-first century and its impact on calcifying organisms. *Nature*, *437*(7059), 681–686. https://doi.org/10.1038/nature04095

Paxian, A., Sein, D. V., Panitz, H. J., Warscher, M., Breil, M., Engel, T., et al. (2016). Bias reduction in decadal predictions of West African monsoon rainfall using regional climate models. *Journal of Geophysical Research: Atmospheres*, *121*, 1715–1735. https://doi.org/10.1002/2015JD024143

Rahmstorf, S., Box, J. E., Feulner, G., Mann, M. E., Robinson, A., Rutherford, S., & Schaffernicht, E. J. (2015). Exceptional twentieth-century slowdown in Atlantic Ocean overturning circulation. *Nature Climate Change*, *5*(5), 475–480. https://doi.org/10.1038/nclimate2554

Roeckner, E., Lautenschlager, M., & Lautenschlager, M.z (2006). IPCC-ar4 mpi-ECHAM5 t63l31 mpiomgr1.5l40, (pre-industrial control experiment): atmosphere 6 hour values mpimet/mad germany, World Data Center for Climate, Deutsches Klimarechenzentrum DKRZ GmbH, Hamburg. https://doi.org/10.1594/WDCC/EH5-T63L31_OM-GR1.5L40_CTL_6H

Sabine, C. L., Feely, R. A., Gruber, N., Key, R. M., Lee, K., Bullister, J. L., et al. (2004). The oceanic sink for anthropogenic CO_2. *Science*, *305*(5682), 367–371. https://doi.org/10.1126/science.1097403

Sein, D. V., Koldunov, N. V., Danilov, S., Sidorenko, D., Wekerle, C., Cabos, W., et al. (2018). The relative influence of atmospheric and oceanic model resolution on the circulation of the North Atlantic Ocean in a coupled climate model. *Journal of Advances in Modeling Earth Systems*, *10*(8), 2026–2041. https://doi.org/10.1029/2018MS001327

Sein, D. V., Koldunov, N. V., Pinto, J. G., & Cabos, W. (2014). Sensitivity of simulated regional Arctic climate to the choice of coupled model domain. *Tellus A: Dynamic Meteorology and Oceanography*, *66*, 23966. https://doi.org/10.3402/tellusa.v66.23966

Sein, D. V., Mikolajewicz, U., Gröger, M., Fast, I., Cabos, W., Pinto, J. G., et al. (2015). Regionally coupled atmosphere-ocean-sea ice-marine biogeochemistry model ROM: 1. Description and validation. *Journal of Advances in Modeling Earth Systems*, *7*, 268–304. https://doi.org/10.1002/2014MS000357

Sgubin, G., Swingedouw, D., Drijfhout, S., Mary, Y., & Bennabi, A. (2017). Abrupt cooling over the North Atlantic in modern climate models. *Nature Communications*, *8*, 14375. https://doi.org/10.1038/ncomms14375

Shaw, T., Baldwin, M., Barnes, E., Caballero, R., Garfinkel, C. I., Hwang, Y.-T., et al. (2016). Storm track processes and the opposing influences of climate change. *Nature Geoscience*, *9*(9), 656–664. https://doi.org/10.1038/ngeo2783

Stammer, D., Ray, R. D., Andersen, O. B., Arbic, B. K., Bosch, W., Carrère, L., et al. (2014). Accuracy assessment of global barotropic ocean tide models. *Reviews of Geophysics*, *52*, 243–282. https://doi.org/10.1002/2014RG000450

Steele, M., Morley, R., & Ermold, W. (2001). PHC: A global ocean hydrography with a high quality Arctic Ocean. *Journal of Climate*, *14*(9), 2079–2087. https://doi.org/10.1175/1520-0442(2001)014<2079:PAGOHW>2.0.CO;2

Steinacher, M., Joos, F., Frölicher, T. L., Bopp, L., Cadule, P., Cocco, V., et al. (2010). Projected 21st century decrease in marine productivity: A multi-model analysis. *Biogeosciences*, *7*(3), 979–1005. https://doi.org/10.5194/bg-7-979-2010

Sura, P., & Newman, M. (2008). The impact of rapid wind variability upon air-sea thermal coupling. *Journal of Climate*, *21*(4), 621–637. https://doi.org/10.1175/2007JCLI1708.1

Sverdrup, H. U. (1953). On conditions for the vernal blooming of phytoplankton. *Journal du Conseil International pour l'Exploration de la Mer*, *18*(3), 287–295. https://doi.org/10.1093/icesjms/18.3.287

Swingedouw, D., Fichefet, T., Goosse, H., & Loutre, M. F. (2009). Impact of transient freshwater releases in the Southern Ocean on the AMOC and climate. *Climate Dynamics*, *33*(2-3), 365–381. https://doi.org/10.1007/s00382-008-0496-1

Thomas, H., Bozec, Y., de Baar, H. J. W., Elkalay, K., Frankignoulle, M., Schiettecatte, L.-S., et al. (2005). The carbon budget of the North Sea. *Biogeosciences*, *2*(1), 87–96. https://doi.org/10.5194/bg-2-87-2005

Thomas, H., Bozec, Y., Elkalay, K., & De Baar, H. J. (2004). Enhanced open ocean storage of CO_2 from shelf sea pumping. *Science*, *304*(5673), 1005–1008. https://doi.org/10.1126/science.1095491

Tibaldi, S., & Molteni, F. (1990). On the operational predictability of blocking. *Tellus A*, *42*(3), 343–365. https://doi.org/10.1034/j.1600-0870.1990.t01-2-00003.x

Ting, M., Kushnir, Y., Seager, R., & Li, C. (2011). Robust features of Atlantic multi-decadal variability and its climate impacts. *Geophysical Research Letters*, *38*, L17705. https://doi.org/10.1029/2011GL048712

Tsunogai, S., Watanabe, S., & Sato, T. (1999). Is there a "continental shelf pump" for the absorption of atmospheric CO_2? *Tellus B*, *51*(3), 701–712. https://doi.org/10.3402/tellusb.v51i3.16468

Ulbrich, U., Pinto, J. G., Kupfer, H., Leckebusch, G. C., Spangehl, T., & Reyers, M. (2008). Changing Northern Hemisphere storm tracks in an ensemble of IPCC climate change simulations. *Journal of Climate*, *21*(8), 1669–1679. https://doi.org/10.1175/2007JCLI1992.1

Valke, S. (2006). *OASIS3 Ocean Atmosphere Sea Ice Soil User's Guide*, *Tech. Rep. TR/CMGC/06/73*. Toulouse, France: CERFACS. http://www.cerfacs.fr/oa4web/papers_oasis/oasis3_UserGuide.pdf

Van Vuuren, D. P., Edmonds, J., Kainuma, M., Riahi, K., Thomson, A., Hibbard, K., et al. (2011). The representative concentration pathways: An overview. *Climatic Change*, *109*(1–2), 5–31. https://doi.org/10.1007/s10584-011-0148-z

Watanabe, M., & Kimoto, M. (2000). Atmosphere-ocean thermal coupling in the North Atlantic: A positive feedback. *Quarterly Journal of the Royal Meteorological Society*, *126*(570), 3343–3369. https://doi.org/10.1002/qj.49712657017

Weedon, G. P., Gomes, S., Viterbo, P., Shuttleworth, W. J., Blyth, E., Österle, H., et al. (2011). Creation of the WATCH forcing data and its use to assess global and regional reference crop evaporation over land during the twentieth century. *Journal of Hydrometeorology*, *12*(5), 823–848. https://doi.org/10.1175/2011JHM1369.1

Xie, S. P., Deser, C., Vecchi, G. A., Collins, M., Delworth, T. L., Hall, A., et al. (2015). Towards predictive understanding of regional climate change. *Nature Climate Change*, *5*(10), 921–930. https://doi.org/10.1038/nclimate2689

Yin, J., Schlesinger, M. E., & Stouffer, R. J. (2009). Model projections of rapid sea-level rise on the northeast coast of the United States. *Nature Geoscience*, *2*(4), 262–266. https://doi.org/10.1038/ngeo462

Zappa, G., Shaffrey, L. C., & Hodges, K. I. (2013). North Atlantic cyclones and model biases in the CMIP5 models. *Journal of Climate*, *26*(15), 5379–5396. https://doi.org/10.1175/JCLI-D-12-00501.1

Zappa, G., Shaffrey, L. C., Hodges, K. I., Sansom, P., & Stephenson, D. (2013). The response of North Atlantic cyclones to climate change in CMIP5 models. *Journal of Climate*, *26*(16), 5846–5862. https://doi.org/10.1175/JCLI-D-12-00573.1

Zhang, J., & Rothrock, D. A. (2003). Modeling global sea ice with a thickness and enthalpy distribution model in generalized curvilinear coordinates. *Monthly Weather Review*, *131*(5), 845–861. https://doi.org/10.1175/1520-0493

Zhang, R. (2017). On the persistence and coherence of subpolar sea surface temperature and salinity anomalies associated with the Atlantic multidecadal variability. *Geophysical Research Letters*, *44*, 7865–7875. https://doi.org/10.1002/2017gl074342

Zhang, R., Sutton, R., Danabasoglu, G., Kwon, Y.-O., Marsh, R., Yeager, S. G., et al. (2019). A review of the role of the Atlantic meridional overturning circulation in Atlantic multidecadal variability and associated climate impacts. *Reviews of Geophysics*, *57*, 316–375. https://doi.org/10.1029/2019RG000644